

# Three-dimensional fast inversion of gravity and its gradient tensor data in wavenumber domain

Sheng Liu<sup>\*1,2,3</sup>, Shi Chen<sup>3</sup>, Honglei Li<sup>3</sup>, Yiju Tang<sup>1</sup>, Fangchao Lu<sup>1</sup>, Changrui Zhou<sup>1</sup>, Quan Lou<sup>1</sup>, Shuanggen Jin<sup>4</sup>, Songbai Xuan<sup>4</sup>, Renbao Yu<sup>5</sup>

<sup>(1)</sup> Henan University of Urban Construction, Pingdingshan, China

<sup>(2)</sup> Hebei Key Laboratory of Earthquake Dynamics, Sanhe, China

<sup>(3)</sup> Institute of Geophysics, China Earthquake Administration, Beijing, China

<sup>(4)</sup> Shanghai Astronomical Observatory, Chinese Academy of Sciences, Shanghai, China

<sup>(5)</sup> Xuchang Seismological Bureau, Xuchang, China

Article history: received January 14, 2025; accepted June 26, 2025

## Abstract

The gravitational potential field plays a pivotal role in interdisciplinary geological exploration. Recently, significant progress has been made in inversion techniques for three-dimensional gravity anomaly and its gradient tensor data in the spatial domain. However, in geoscientific research, gravity anomalies derived from models such as the Earth Gravitational Model (EGM) and other characteristic series models are prevalent. These spherical harmonic models have limitations due to their finite order, which can lead to truncation errors when traditional spatial domain inversion methods are applied. To address this problem, this paper presents a novel inversion method for three-dimensional gravity and its gradient tensor data in the wavenumber domain. Unlike the spatial domain inversion, the Green's function matrix in the wavenumber domain is sparse, resulting in substantial improvements in computational efficiency and reduced calculation time. Furthermore, to tackle the issue of multiple solutions often encountered in wavenumber domain inversions, regularization techniques commonly used in the spatial domain have been incorporated. This strategic integration stabilizes the inversion process and enhances the reliability of the results. To validate the effectiveness of the proposed method, rigorous testing using theoretical model data and field data has been performed. The inversion results clearly demonstrate the robustness of this novel approach, making it highly suitable for inverting three-dimensional gravity anomalies and their gradient tensor data.

Keywords: Gravity Anomaly; Gradient Tensor Data; Wavenumber Domain; Inversion

---

## 1. Introduction

Gravity inversion serves as a fundamental technique for exploring crustal or lithospheric structure and earth's evolution. Traditionally, three-dimensional gravity inversion has been primarily conducted within the spatial domain (Li and Oldenburg, 1996; 1998). By utilizing Green's function matrix, also known as the kernel matrix,

a linear relationship can be formulated between the discretized field source model and the observed gravity anomaly. However, when addressing three-dimensional issues, the kernel matrix tends to be dense and large-scale. This characteristic of the potential field results in a significant computational burden.

Considerable research endeavors focus on optimizing the efficiency of large-scale gravity inversion. The Equivalent Geometric Framework technique notably decreases computational expenses (Yao et al., 2003, 2007). Wavelet transform algorithms compress kernel matrices, minimizing storage needs for redundant and insignificant data, thereby alleviating computational loads (Li and Oldenburg, 2003; Davis and Li, 2011). Transitioning inversion from model space to data space facilitates swift joint inversion processes (Zhang et al., 2022). Dense kernel matrices can be decomposed using the Randomized Singular Value Decomposition (RSVD) method (Vatankhah et al., 2018). By segmenting gravity data into subsets and leveraging deep learning, rapid inversion of extensive gravity datasets becomes feasible (Huang et al., 2022). Leveraging MPI and GPU acceleration technologies enables large-scale, rapid inversion (Cuma et al., 2014; Hou et al., 2016). While parallel computing significantly boosts computational speeds, it also demands considerable computational resources. Thus, the ongoing challenge is to enhance inversion efficiency while minimizing resource consumption.

Furthermore, the development of three-dimensional gravity inversion in the space domain has reached a considerable level. However, spherical harmonic gravity anomaly models, including the EGM, the EIGEN series global and/or regional gravity field models, have been frequently utilized to explore geoscience problems (Pavlis et al., 2008; 2012; Hirt et al., 2013). It should be noted that if the traditional 3D inversion approach in the space domain is employed, truncation errors will inevitably be introduced due to the inherent finite order of the harmonic model. This limitation can potentially impact the accuracy and reliability of the geoscientific interpretations.

Compared to forward and inversion in the spatial domain, forward and inversion in the wavenumber domain offers advantages such as efficient computational capabilities, lower memory consumption, and convenient formula expression (Cui and Guo, 2019; Zhao et al., 2019). A forward method for gravity and magnetic anomalies of inhomogeneous undulating layers in the wavenumber domain (Parker, 1973) and the wavenumber-domain forward formulas for gravity and magnetic anomalies of inhomogeneous horizontal layers (Blakely, 1995) are introduced. Xu et al. (2018) proposed a forward method in the wavenumber domain for three-dimensional fault models. Dai et al. (2019; 2020) combined the advantages of the spatial and wavenumber domains to develop a rapid forward method for mixed gravity anomalies. Hogue et al. (2020) integrated the Block Toeplitz Toeplitz Block (BTTB) structure with the Fast Fourier Transform (FFT) to develop an efficient forward method in the wavenumber domain.

In recent years, significant progress has been made in the development of wavenumber-domain inversion methods. Jing et al. (2019) proposed a rapid forward method in the wavenumber domain for vertically layered media, significantly enhancing the efficiency of large-scale inversions. Renaut et al. (2020) leveraged the BTTB structure of the gravity sensitivity matrix, utilized the Fast Fourier Transform (FFT) for the computation of the kernel matrix and its transpose, reducing memory requirements. Additionally, the fast cross-gradient (Vatankhah, 2022) and reweighted Gramian-constrained joint inversions (Saeed, 2022) have been developed in the wavenumber domain. These inversion methods employ layered forward in the wavenumber domain, effectively conserving computational memory and improving efficiency. Layered forward in the wavenumber domain necessitates multiple applications of the FFT followed by an inverse FFT to convert the forward results from the wavenumber domain to the spatial domain, where the inversion is subsequently performed. Furthermore, although large dense kernel matrices can be decomposed to reduce computational dimensionality, the decomposed matrices remain substantial in size, leading to high computational costs.

To tackle the aforementioned challenges, this paper introduces a inversion method for gravity anomaly and its gradient tensor data in the full-wavenumber domain, blending the wavenumber-domain forward approach for gravity anomaly data with traditional spatial-domain inversion methods. Initially, this paper offers an analytical formula for rectangular prism elements within the wavenumber domain. Utilizing this formula to formulate Green's matrices for the discretized field source model results in matrices that can be transformed into a three-matrix multiplication form, offering sparsity compared to the space-domain representation. The second section elaborates on the comprehensive methodology proposed herein. Furthermore, the third section utilizes synthetic and filed data to evaluate the feasibility of this approach. The final section discusses the recognized strengths and limitations of this method, along with potential future applications and development directions.

## 2. Methodology

When the meshing units are rectangular prisms, the calculation formula for the gravity anomaly  $\Delta g$  at any point in the spatial domain can be expressed as (Nagy, 1996):

$$\Delta g(x, y, z) = G\Delta\rho \left\{ \begin{array}{l} -(x - \xi) \ln[(y - \eta) + R] - (y - \eta) \ln[(x - \xi) + R] \\ + (z - h) \tan^{-1} \frac{(x - \xi)(y - \eta)}{(z - h)} \end{array} \right\} \left. \begin{array}{l} \xi_0 + a \\ \xi_0 - a \end{array} \right| \left. \begin{array}{l} \eta_0 + b \\ \eta_0 - b \end{array} \right| h_1 \Big| h_0 \quad (1)$$

where,  $G$  is the universal gravitational constant,  $\Delta\rho$  is the density anomaly,  $R = \sqrt{(\xi - x)^2 + (\eta - y)^2 + (h - z)^2}$  is the distance between the field source and the observation point,  $x$ ,  $y$ , and  $z$  are the coordinates of the observation point,  $\xi$ ,  $\eta$ , and  $h$  are the coordinates of the density partition unit,  $h_0$  and  $h_1$  are the coordinates of any meshing unit in the depth direction, and  $2a$  and  $2b$  are the lengths of the meshing units in the  $x$  and  $y$  directions, respectively.

The forward formula for gravity anomaly  $\Delta g$  in spatial domain can usually be expressed as,

$$\mathbf{A}\mathbf{m} = \mathbf{g} \quad (2)$$

where,  $\mathbf{m}$  and  $\mathbf{g}$  represent the density anomaly model and observed gravity anomaly, respectively, and  $\mathbf{A}$  represents the dense kernel matrix. The linear relationship can be established between the field source and gravity anomalies and their gradient tensors according to the previous researches (Nagy et al., 1996; 2000; 2002). This paper introduced the linear relationship in the wavenumber domain as the Eq. (3).

$$\mathbf{A}_f \mathbf{m} = \mathbf{g}_f, \quad (3)$$

where, the  $\mathbf{A}_f$  represents the Green's function matrices, and  $\mathbf{g}_f$  represents the spectrum of gravity anomaly computed from the Fourier transform.

### 2.1 Gravity anomaly of the rectangular prism in the wavenumber domain

On the same horizontal plane, the gravity anomaly in the wavenumber domain can be derived through a two-dimensional Fourier transform ( $F[\ ]$ ).

$$\mathbf{g}_f = F(\mathbf{g}) = \iint \mathbf{g} e^{-i(ux+vy)} dx dy \quad (4)$$

where,  $i = \sqrt{-1}$ ,  $u$  and  $v$  are the wavenumbers in the  $x$  and  $y$  directions, respectively. If the observed point locates on the plane of  $z = z_0$ , the gravitational potential in the wavenumber domain can be written as follows. For the detailed derivation process, please refer to the appendix.

$$\begin{aligned} \mathbf{U}(u, v) &= \frac{2\pi G\Delta\rho}{w} \frac{4 \sin(ua) \sin(vb) e^{wz_0} (e^{-wh_0} - e^{-wh_1})}{uvw} e^{-i(\xi_0 u + \eta_0 v)} \\ &= 8\pi G\Delta\rho \frac{e^{wz_0} (e^{-wh_0} - e^{-wh_1}) \sin(ua)}{w^2} \frac{1}{u} e^{-i\xi_0 u} \frac{\sin(vb)}{v} e^{-i\eta_0 v} \end{aligned} \quad (5)$$

where,  $\mathbf{U}$  is the gravitational potential in the spatial domain,  $w = \sqrt{u^2 + v^2}$ . When  $z_0 = 0$ , the multiplication form

of the forward calculation of the gravity anomaly in the wavenumber domain of the rectangular model can be obtained, which can be expressed as,

$$\begin{aligned} \mathbf{U}(u, v) &= \frac{2\pi G\Delta\rho}{w} \frac{4 \sin(ua) \sin(vb) (e^{-wh_0} - e^{-wh_1})}{uvw} e^{-i(\xi_0 u + \eta_0 v)} \\ &= 8\pi G\Delta\rho \frac{(e^{-wh_0} - e^{-wh_1}) \sin(ua)}{w^2} \frac{1}{u} e^{-i\xi_0 u} \frac{\sin(vb)}{v} e^{-i\eta_0 v} \end{aligned} \quad (6)$$

In the wavenumber domain, there is a conversion relationship between gravity anomaly and gravity potential as follows,

$$\mathbf{g} = \mathbf{U}_z = F^{-1}[w \cdot \mathbf{U}(u, v)] \quad (7)$$

Considering the division of underground sources into multiple layers, after deduction, the wavenumber-domain gravity potential of any partition unit in the  $L$ -th layer ( $L = 0, 1, 2, \dots, Nz-1$ ) at the observed point can be expressed as,

$$\mathbf{U}_L(u, v) = 8\pi G\Delta\rho \frac{(e^{-wh_0} - e^{-wh_1})}{w^2} e^{-Lw\Delta h} \frac{\sin(ua)}{u} e^{-i\xi_0 u} \frac{\sin(vb)}{v} e^{-i\eta_0 v} \quad (8)$$

where,  $\Delta h = h_1 - h_0$ .

Then, the gravity anomaly in the wavenumber domain of the observed point can be further transformed as follows,

$$\mathbf{g}(u, v) = 8\pi G\Delta\rho \frac{(e^{-wh_0} - e^{-wh_1})}{w} e^{-Lw\Delta h} \frac{\sin(ua)}{u} e^{-i\xi_0 u} \frac{\sin(vb)}{v} e^{-i\eta_0 v} \quad (9)$$

Additionally, in the wavenumber domain, the six independent gradient tensor components of the gravitational potential  $\mathbf{U}_T$  can be expressed as following form,

$$\mathbf{U}_T = \begin{bmatrix} \mathbf{U}_{xx} & \mathbf{U}_{xy} & \mathbf{U}_{xz} \\ & \mathbf{U}_{yy} & \mathbf{U}_{yz} \\ & & \mathbf{U}_{zz} \end{bmatrix} = \begin{bmatrix} -u^2 \mathbf{U} & -uv \mathbf{U} & iuw \mathbf{U} \\ & -v^2 \mathbf{U} & ivw \mathbf{U} \\ & & w^2 \mathbf{U} \end{bmatrix}. \quad (10)$$

Furthermore, the calculation formula in the wavenumber domain of the gravity tensor data can be obtained as follows.

$$\begin{cases} \mathbf{g}_{xx}(u, v) = -8\pi G\Delta\rho \frac{(e^{-wh_0} - e^{-wh_1})}{w^2} e^{-Lw\Delta h} u \sin(ua) e^{-i\xi_0 u} \frac{\sin(vb)}{v} e^{-i\eta_0 v} \\ \mathbf{g}_{xy}(u, v) = -8\pi G\Delta\rho \frac{(e^{-wh_0} - e^{-wh_1})}{w^2} e^{-Lw\Delta h} \sin(ua) e^{-i\xi_0 u} \sin(vb) e^{-i\eta_0 v} \\ \mathbf{g}_{xz}(u, v) = 8\pi G\Delta\rho \frac{(e^{-wh_0} - e^{-wh_1})}{w} e^{-Lw\Delta h} i \cdot \sin(ua) e^{-i\xi_0 u} \frac{\sin(vb)}{v} e^{-i\eta_0 v} \\ \mathbf{g}_{yy}(u, v) = -8\pi G\Delta\rho \frac{(e^{-wh_0} - e^{-wh_1})}{w^2} e^{-Lw\Delta h} \frac{\sin(ua)}{u} e^{-i\xi_0 u} v \sin(vb) e^{-i\eta_0 v} \\ \mathbf{g}_{yz}(u, v) = 8\pi G\Delta\rho \frac{(e^{-wh_0} - e^{-wh_1})}{w} e^{-Lw\Delta h} \frac{\sin(ua)}{u} e^{-i\xi_0 u} i \cdot \sin(vb) e^{-i\eta_0 v} \\ \mathbf{g}_{zz}(u, v) = 8\pi G\Delta\rho (e^{-wh_0} - e^{-wh_1}) e^{-Lw\Delta h} \frac{\sin(ua)}{u} e^{-i\xi_0 u} \frac{\sin(vb)}{v} e^{-i\eta_0 v} \end{cases} \quad (11)$$

## Gravity-gradient tensor wavenumber inversion

The implementation requires predefining a wavenumber-domain cutoff frequency for effective spectral analysis. Assume that the sampling points in the horizontal  $x$  and  $y$  directions are predetermined. The frequency range of  $u$  and  $v$  can be computed with Eq. (12), while Eq. (13) is used to determine the sampling intervals of the wavenumbers.

$$u \in \left[-\frac{1}{2\Delta x}, \frac{1}{2\Delta x}\right], v \in \left[-\frac{1}{2\Delta y}, \frac{1}{2\Delta y}\right] \quad (12)$$

$$du = \frac{1}{m\Delta x}, v = \frac{1}{n\Delta y} \quad (13)$$

Here,  $\Delta x$  and  $\Delta y$  are the  $x$  and  $y$  grid intervals in the space domain, and  $m$  and  $n$  are the number of sampling points in the  $x$  and  $y$  directions, respectively.

### 2.2 Green's matrices in the wavenumber domain

From Eq. (9), the kernel matrix in the wavenumber domain can be decomposed into the following formula.

$$A_f = cWW_LK \quad (14)$$

where,  $c = 8\pi G$ , the matrix  $W$  is composed of  $\frac{(e^{-w_i h_0} - e^{-w_i h_1})}{w_i}$ , the matrix  $W_L$  is composed of  $e^{-Lw_i \Delta h}$ , and

the matrix  $K$  is composed of  $\frac{\sin(u_j a)}{u_j} e^{-i\xi_p u_j} \frac{\sin(v_k b)}{v_k} e^{-i\eta_q v_k}$ .  $W = \begin{bmatrix} W_1 & 0 & 0 & \dots \\ 0 & W_2 & 0 & \vdots \\ 0 & 0 & W_3 & \vdots \\ \vdots & \vdots & \vdots & \ddots \end{bmatrix}$ ,  $W_i = \frac{(e^{-w_i h_0} - e^{-w_i h_1})}{w_i}$ ,

$W_i = \sqrt{u_j^2 + v_k^2}$ ,  $i = Nx * j + k$ ,  $Nx$  is the number of  $u$ , which is only related to the wave number and independent

of the  $Z$  direction.  $W_L = \begin{bmatrix} W_L^1 & 0 & 0 & \dots \\ 0 & W_L^2 & 0 & \vdots \\ 0 & 0 & W_L^3 & \vdots \\ \vdots & \vdots & \vdots & \ddots \end{bmatrix}$ ,  $W_L^j = e^{-Lj w_i \Delta h}$ ,  $j = 0, 1, 2, \dots, Nz - 1$ .  $K = \begin{bmatrix} A \otimes B & 0 & 0 & \dots \\ 0 & A \otimes B & 0 & \vdots \\ 0 & 0 & A \otimes B & \vdots \\ \vdots & \vdots & \vdots & \ddots \end{bmatrix}$ ,

where,  $A = \frac{\sin(u_j a)}{u_j} e^{-i\xi_p u_j}$ ,  $j = 1, 2, 3, \dots, Nx$ ,  $p = 1, 2, 3, \dots, Nx$ .  $B = \frac{\sin(v_k b)}{v_k} e^{-i\eta_q v_k}$ ,  $k = 1, 2, 3, \dots, Ny$ ,  $q = 1, 2, 3, \dots, Ny$ ,  $\otimes$

represents the Kronecker product. Subsequently, the following equation can be obtained.

$$A_f m = (cWW_LK)m = g_f \quad (15)$$

From Eqs. (9), (10), and (15), the forward formula for the gravity tensor data in the wavenumber domain can be further acquired.

$$\begin{cases} A_f^{xx} m = (cW^{xx} W_L^{xx} W^{xx})m = g_f^{xx} \\ A_f^{xy} m = (cW^{xy} W_L^{xy} W^{xy})m = g_f^{xy} \\ A_f^{xz} m = (cW^{xz} W_L^{xz} W^{xz})m = g_f^{xz} \\ A_f^{yy} m = (cW^{yy} W_L^{yy} W^{yy})m = g_f^{yy} \\ A_f^{yz} m = (cW^{yz} W_L^{yz} W^{yz})m = g_f^{yz} \\ A_f^{zz} m = (cW^{zz} W_L^{zz} W^{zz})m = g_f^{zz} \end{cases} \quad (16)$$

where,  $g_f^{xx}$ ,  $g_f^{xy}$ ,  $g_f^{xz}$ ,  $g_f^{yy}$ ,  $g_f^{yz}$  and  $g_f^{zz}$  represent the gravity tensor data calculated using Fourier transform,  $A_f^{xx}$ ,  $A_f^{xy}$ ,  $A_f^{xz}$ ,  $A_f^{yy}$ ,  $A_f^{yz}$  and  $A_f^{zz}$  represent the kernel matrices of the tensor after Fourier transform, and  $W^{xx}$ ,  $W^{xy}$ ,  $W^{xz}$ ,  $W^{yy}$ ,  $W^{yz}$ ,  $W^{zz}$ ,  $W_L^{xx}$ ,  $W_L^{xy}$ ,  $W_L^{xz}$ ,  $W_L^{yy}$ ,  $W_L^{yz}$ ,  $W_L^{zz}$ ,  $K^{xx}$ ,  $K^{xy}$ ,  $K^{xz}$ ,  $K^{yy}$ ,  $K^{yz}$ ,  $K^{zz}$  represent matrices similar to  $W$ ,  $W_L$ ,  $K$  in Eq. (15).

### 2.3 Tikhonov regularization

Gravity inversion is a typical multi solution problem, and adding regularization constraints can effectively improve multi solution. Therefore, this paper incorporates regularization constraints from spatial-domain inversion methods into Eq. (15), thereby formulating the objective function for the wavenumber-domain inversion of gravity anomaly data as follows.

$$\Phi = \|A_f \mathbf{m} - \mathbf{g}_f\|_2^2 + \lambda \|\mathbf{m}\|_2^2, \quad (17)$$

where,  $\Phi$  represents the objective function, and  $\lambda$  represents the regularization parameter. In addition, the L-curve method in the spatial domain is used to obtain the optimal regularization parameters  $\lambda$ . Additionally, the least squares method is used to solve the objective function shown in Eq. (18). Furthermore, the following equation can be obtained,

$$\begin{bmatrix} A_f \\ \lambda I \end{bmatrix} \mathbf{m} = \begin{bmatrix} \mathbf{g}_f \\ 0 \end{bmatrix} \quad (18)$$

where  $I$  represents a standard matrix. Moreover, the least square solution of Eq. (18) can be written as,

$$\mathbf{m} = (A_f^T A_f + \lambda^2 I)^{-1} A_f^T \mathbf{g}_f. \quad (19)$$

Apparently, the aforementioned least squares inversion technique can equally be utilized for inverting gravity gradient tensor data. The primary difference in performing 3D gravity inversion within the wavenumber

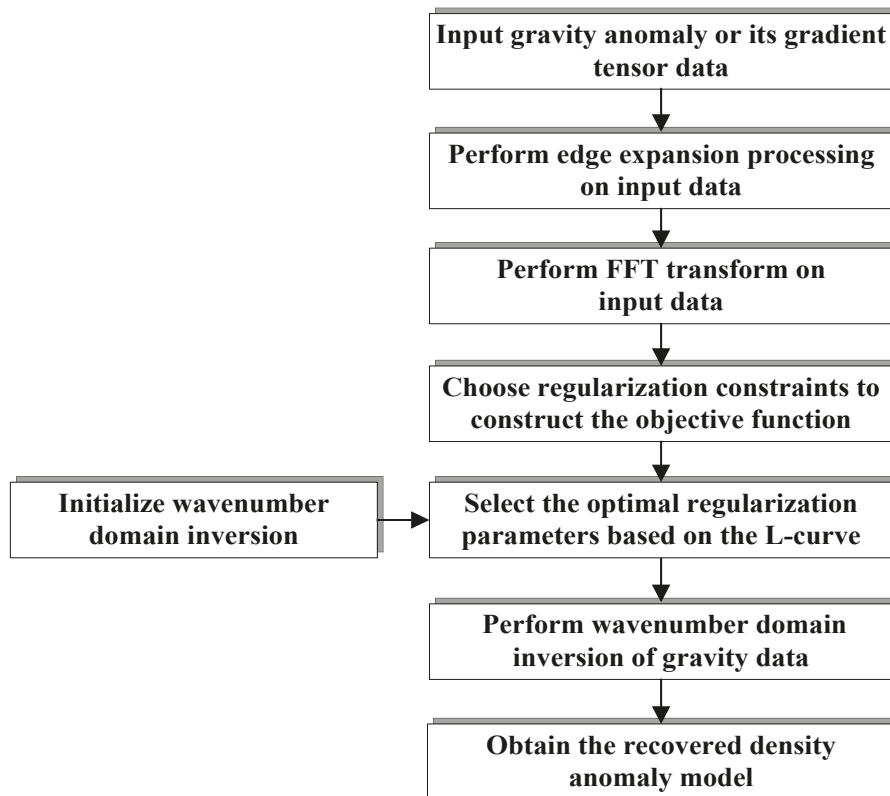


**Figure 1.** The workflow for wavenumber-domain inversion for gravity anomaly data.

domain hinges on the unique properties of the new Green's function matrix, which is characterized by sparsity and reduced dimensionality. It is evident that prior studies on regularization and constraint methodologies are equally pertinent to this inversion process in the wavenumber domain.

Furthermore, the fundamental workflow of the wavenumber-domain inversion for gravity anomalies and their gradient tensor data, as introduced in this paper, is showed in Fig. 1, which can be described as follows. Firstly, inputting gravity anomaly or gravity gradient tensor data. Then, applying edge extension processing to the input gravity data to ensure the number of observations meets the FFT requirements. The edge expansion method used in this paper is zero value edge expansion. Then, transforming the extended spatial-domain gravity data into the wavenumber domain using the FFT. Then, a minimum-norm regularization technique is adopted to formulate the objective function presented in Eq. (17). Next, the wavenumber-domain inversion is initialized, and obtaining the optimal regularization parameter  $\lambda$  determined by the L-curve. Finally, substitute the regularization parameter  $\lambda$  into Eq. (19) to execute the inversion and obtain the recovered density anomaly model  $m$ .

### 3. Results and validation

#### 3.1 Synthetic model test

All testing of the method introduced in this paper was conducted solely on a laptop equipped with 16GB of RAM, an i7-9750H CPU (base clock speed of 2.6 GHz), and a GeForce GTX 1660 Ti GPU. The proposed algorithm was implemented using Python 3, without employing any parallel computing methods.

To evaluate the validity of our approach within the wavenumber domain, as detailed in Section 2, we utilized synthetic models. Synthetic model one comprises three blocks of residual density, as depicted in Fig. 2. In this paper, the units for density anomaly are  $\text{g/cm}^3$ , and the units for gravity anomaly are the internationally accepted gravity units  $\text{g.u.}$ . In this paper, the term "density anomaly" refers to the deviation between the source density and the background reference density. Additionally, the high-density anomaly values (e.g.  $2.0 \text{ g/cm}^3$ ) displayed in Fig. 2 and the subsequent synthetic models are solely intended to validate the accuracy of the method proposed in this paper.

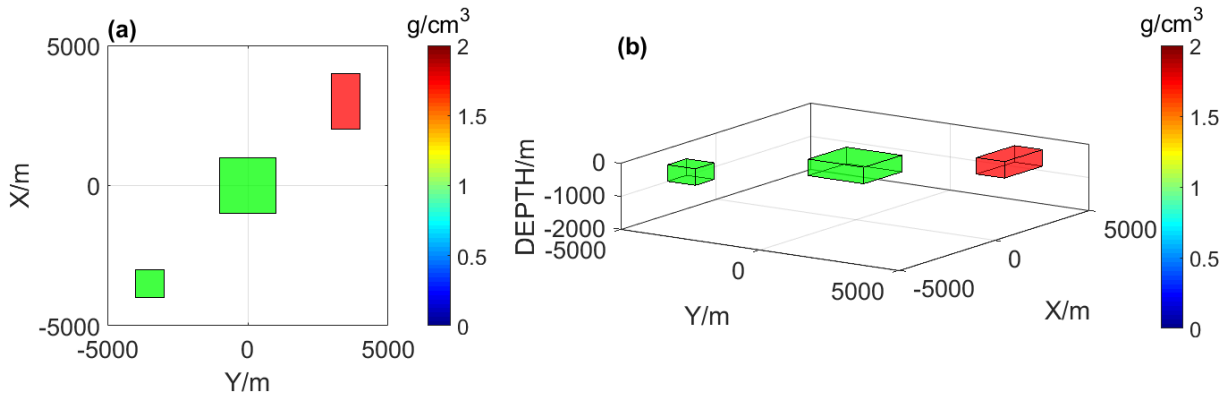


**Figure 2.** Schematic diagram of field source with density anomaly of synthetic model 1. (a) Top view of the spatial three-dimensional distribution of density anomaly model, (b) The spatial three-dimensional distribution of density anomaly model.

The forward gravity anomaly and its gradient tensor data in space domain shown in Fig. 3 are calculated based on the previous research by Nagy et al. (2000; 2002).

Then, the gravity anomaly and its tensor data in the wavenumber domain were calculated, as shown in Fig. 4. Notably, these results closely resemble the forward anomaly outcomes presented in the spatial domain in Fig. 3.

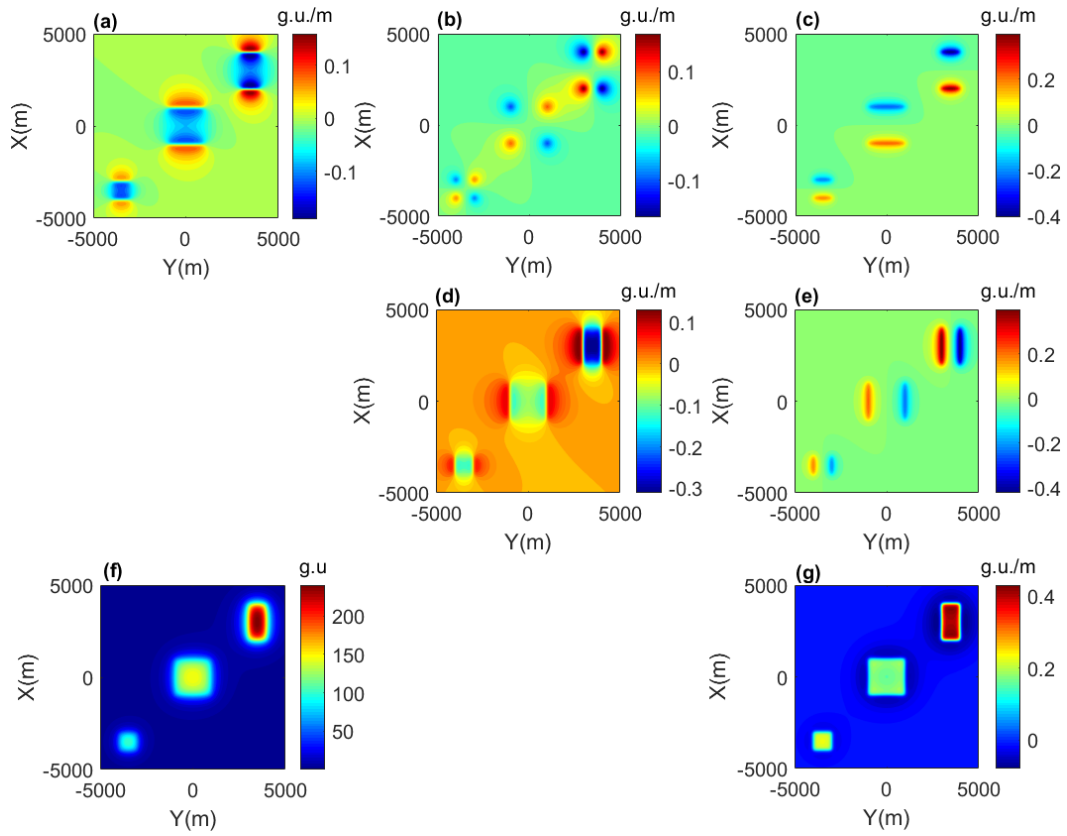


**Figure 3.** Gravity forward anomaly by the space domain method. (a)  $g_{xx}$ , (b)  $g_{xy}$ , (c)  $g_{xz}$ , (d)  $g_{yy}$ , (e)  $g_{yz}$ , (f)  $g_z$ , (g)  $g_{zz}$ .

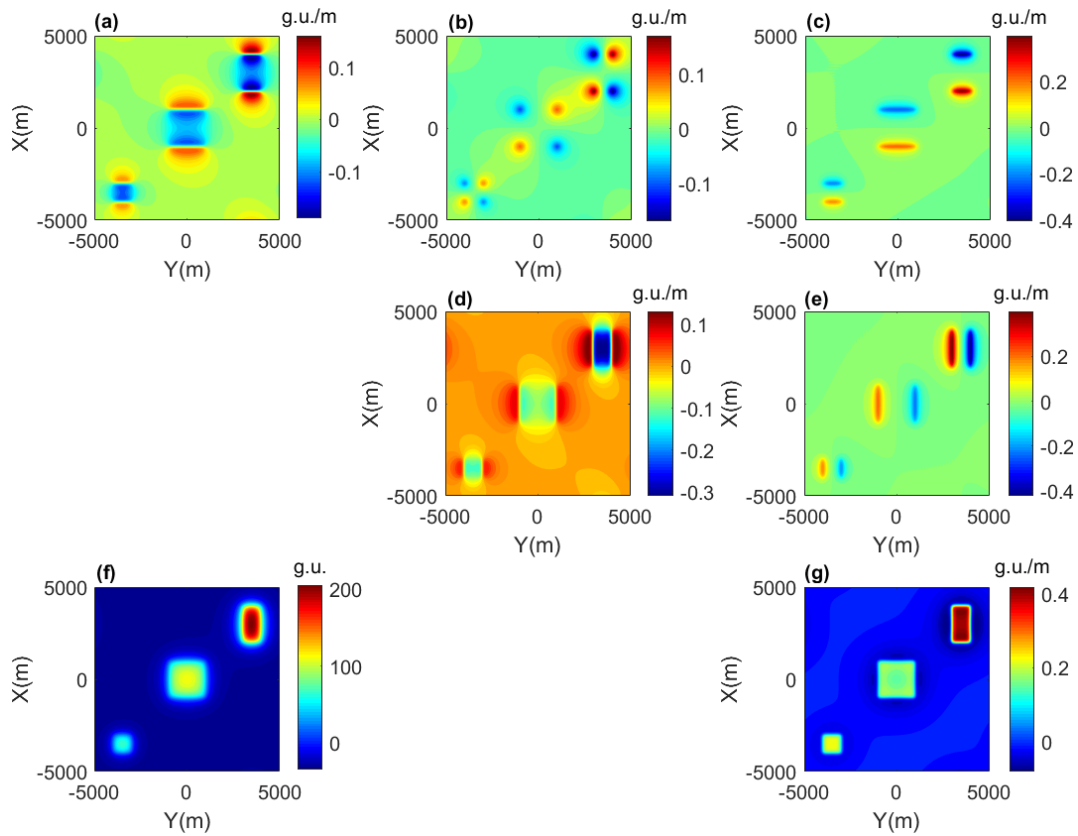


**Figure 4.** Gravity forward anomaly by the wavenumber domain method. (a)  $g_{xx}$ , (b)  $g_{xy}$ , (c)  $g_{xz}$ , (d)  $g_{yy}$ , (e)  $g_{yz}$ , (f)  $g_z$ , (g)  $g_{zz}$ .

Then, Fig. 5 presents the result obtained by subtracting the gravity anomaly and gradient tensor data in the wavenumber domain from those in the spatial domain, indicating that the two results are very close. It can verify the correctness of the forward of gravity anomalies and their gradient tensor data in the wavenumber domain. Additionally, compared to forward in the spatial domain, the wavenumber domain method is better suited for gravity potential anomaly models represented by finite-order spherical harmonics, especially when handling gridded or filtered data.

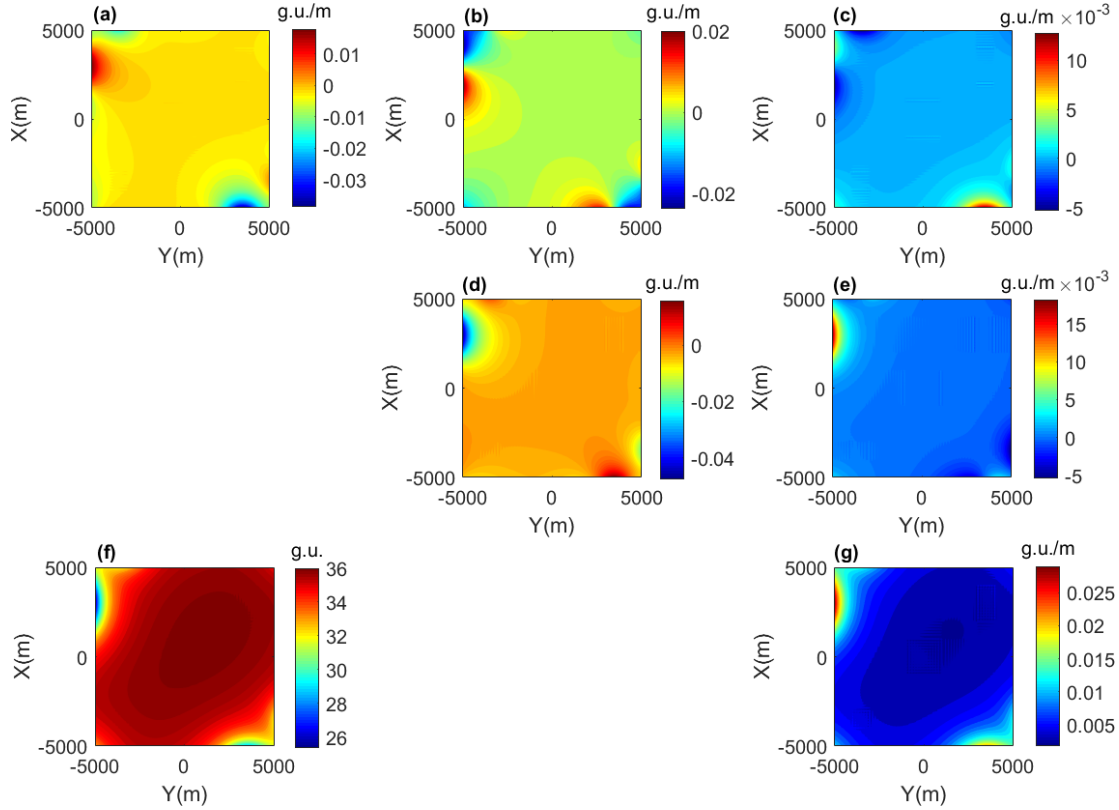


**Figure 5.** The difference between gravity forward anomaly by two approaches of model 1. (a)  $g_{xx}$ , (b)  $g_{xy}$ , (c)  $g_{xz}$ , (d)  $g_{yy}$ , (e)  $g_{yz}$ , (f)  $g_z$ , (g)  $g_{zz}$ .

We further employed synthetic model 2 to validate the correctness of the wavenumber-domain forward and inverse methods proposed in this paper. The spatial distribution of synthetic model 2, which also incorporates three density anomalies, is illustrated in Fig. 6.

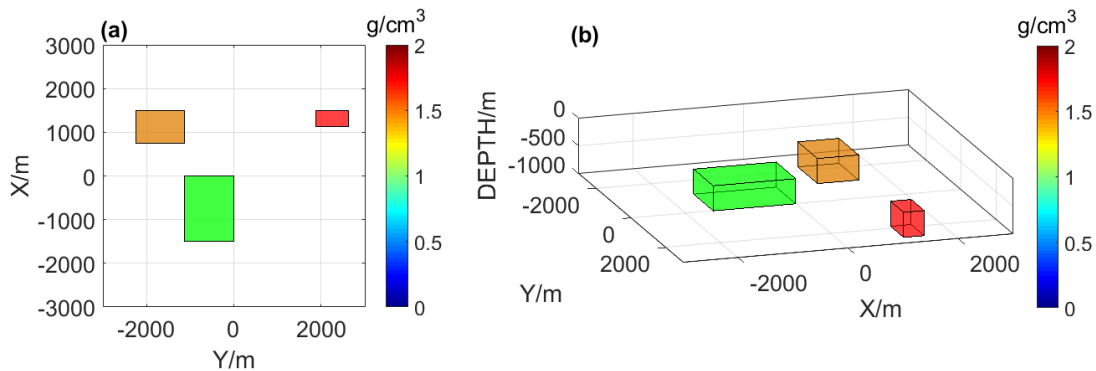


**Figure 6.** Schematic diagram of field source with density anomaly of synthetic model 2. (a) Top view of the spatial three-dimensional distribution of density anomaly model, (b) The spatial three-dimensional distribution of density anomaly model.

Furthermore, Figs. 7 and 8 respectively present the forward gravity anomaly and gradient tensor data of synthetic model 2 in both the spatial domain and wavenumber domain.

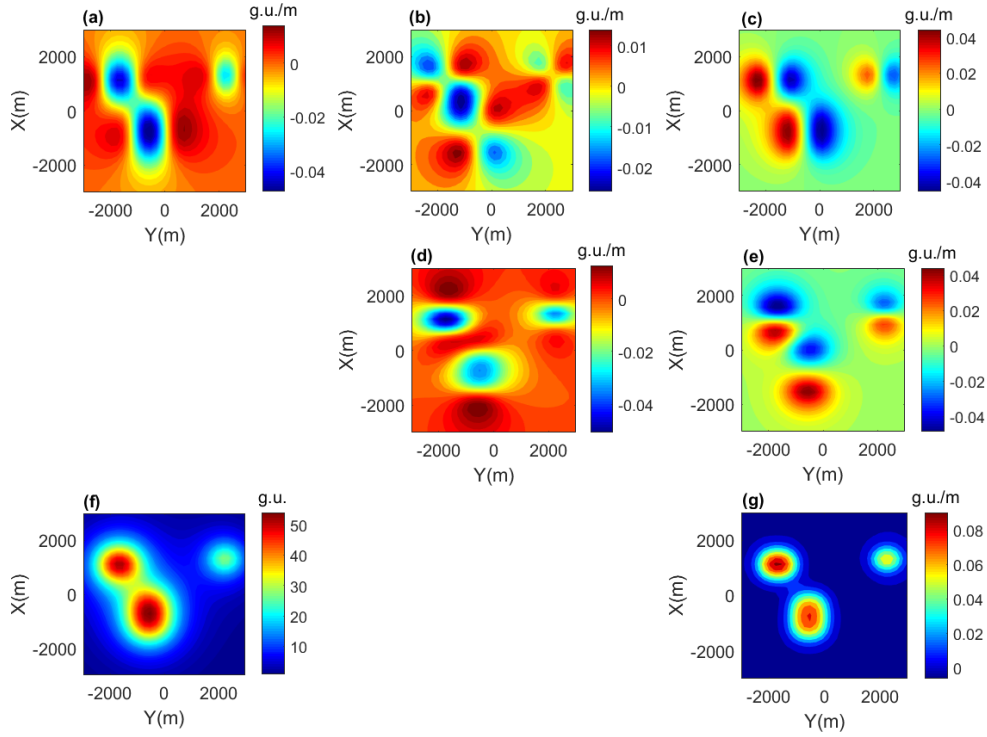


**Figure 7.** Gravity forward anomaly by the space domain method of synthetic model 2. (a)  $g_{xx}$ , (b)  $g_{xy}$ , (c)  $g_{xz}$ , (d)  $g_{yy}$ , (e)  $g_{yz}$ , (f)  $g_z$ , (g)  $g_{zz}$

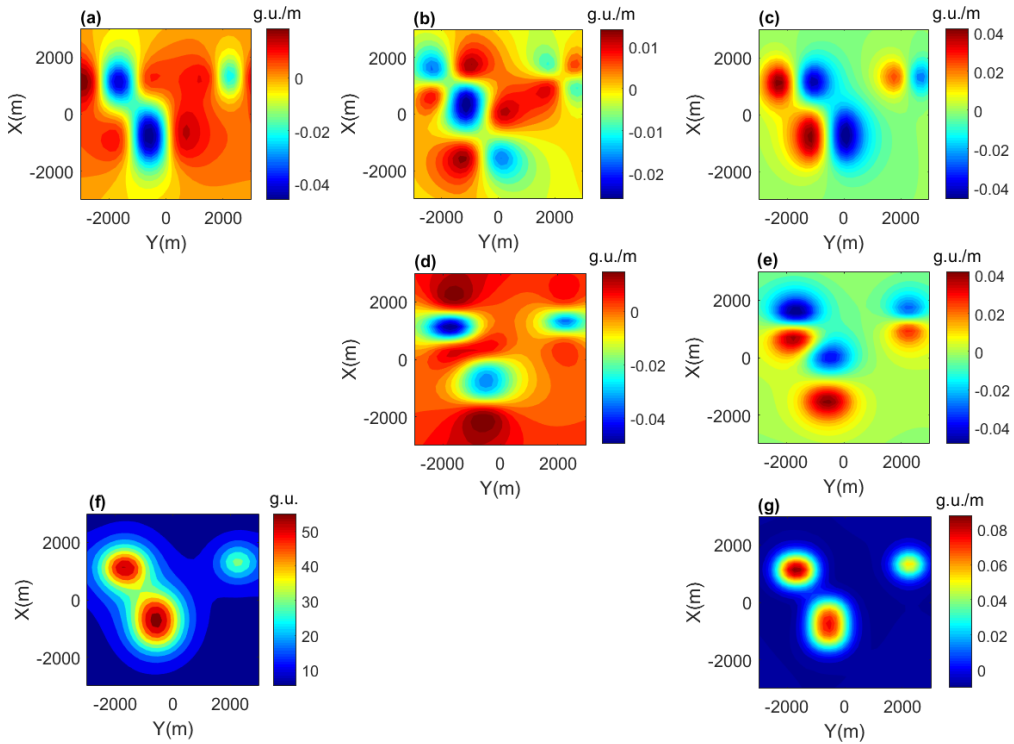


**Figure 8.** Gravity forward anomaly by the wavenumber domain method of synthetic model 2. (a)  $g_{xx}$ , (b)  $g_{xy}$ , (c)  $g_{xz}$ , (d)  $g_{yy}$ , (e)  $g_{yz}$ , (f)  $g_z$ , (g)  $g_{zz}$

We then compared the forward results of synthetic model 2 in both spatial and wavenumber domains, with the differences illustrated in Fig. 9. As can be observed, the discrepancy values shown in Fig. 9 are relatively minor, which further validates the accuracy of the wavenumber-domain forward method proposed in this paper.

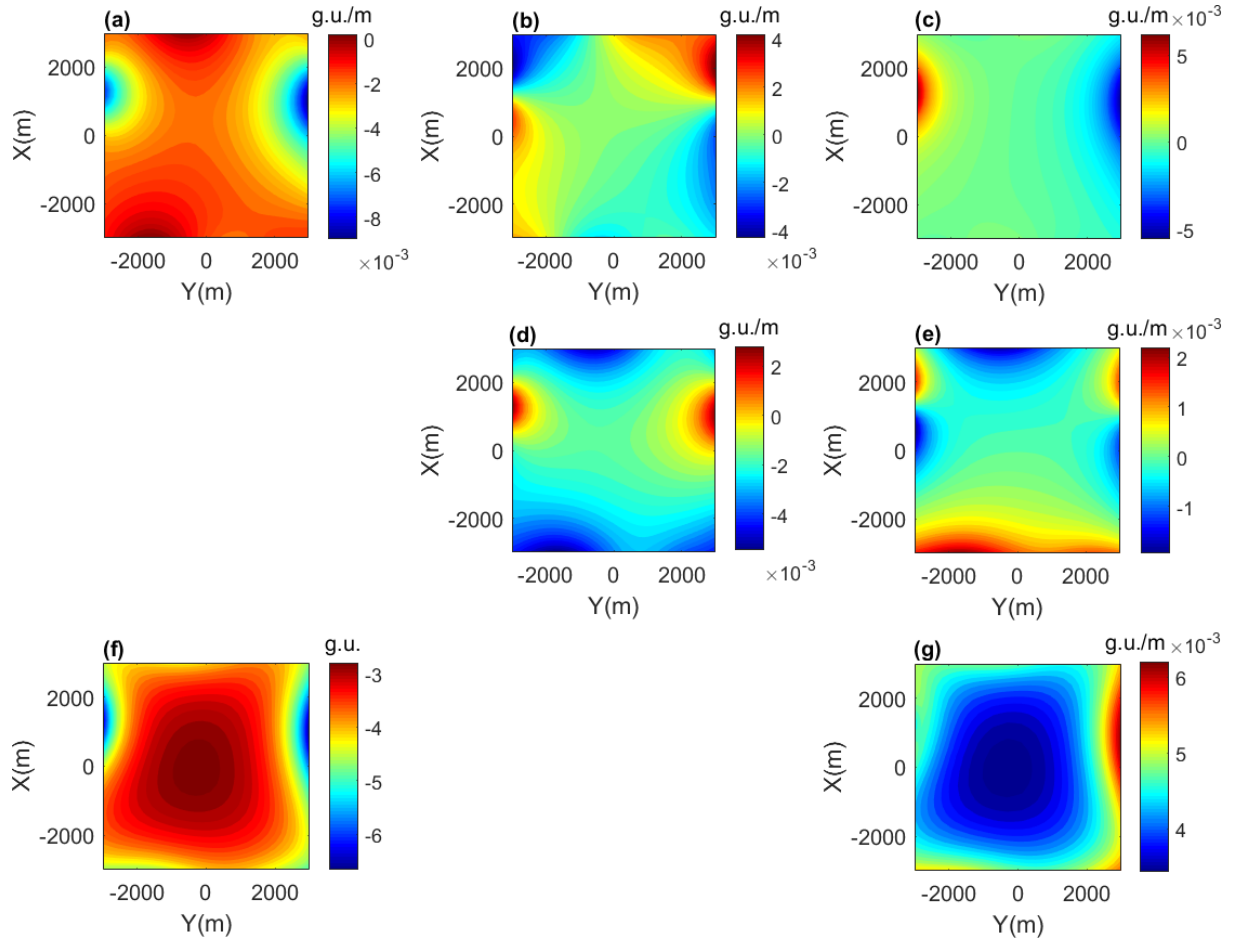


**Figure 9.** The difference between gravity forward anomaly by two approaches of synthetic model 2. (a)  $g_{xx}$ , (b)  $g_{xy}$ , (c)  $g_{xz}$ , (d)  $g_{yy}$ , (e)  $g_{yz}$ , (f)  $g_z$ , (g)  $g_{zz}$ .

Next, we will utilize the forward data from synthetic model 2 shown in Fig. 8 to validate the wavenumber-domain inversion method proposed in this paper. First, we will select appropriate regularization parameters based on the gravity anomalies and gradient tensor data shown in Fig. 8 by L-curves method, which will then be applied to the subsequent wavenumber-domain inversion. Figure 10 illustrates the variation characteristics of both model error and data error with respect to various regularization parameters  $\lambda$ . For the data error component, a comparison is made between the power spectrum error and the corresponding spatial domain data error. The results reveal that both trends are identical, and they share the same optimal regularization parameters. According to the Generalized Cross Validation (GCV) method (Farquharson and Oldenburg, 2004), the trade-off regularization parameter in this context represents the optimal choice. The result shown in Fig. 10 demonstrates that the L-curve method for selecting appropriate regularization parameters is equally applicable to the wavenumber-domain inversion proposed in this paper.

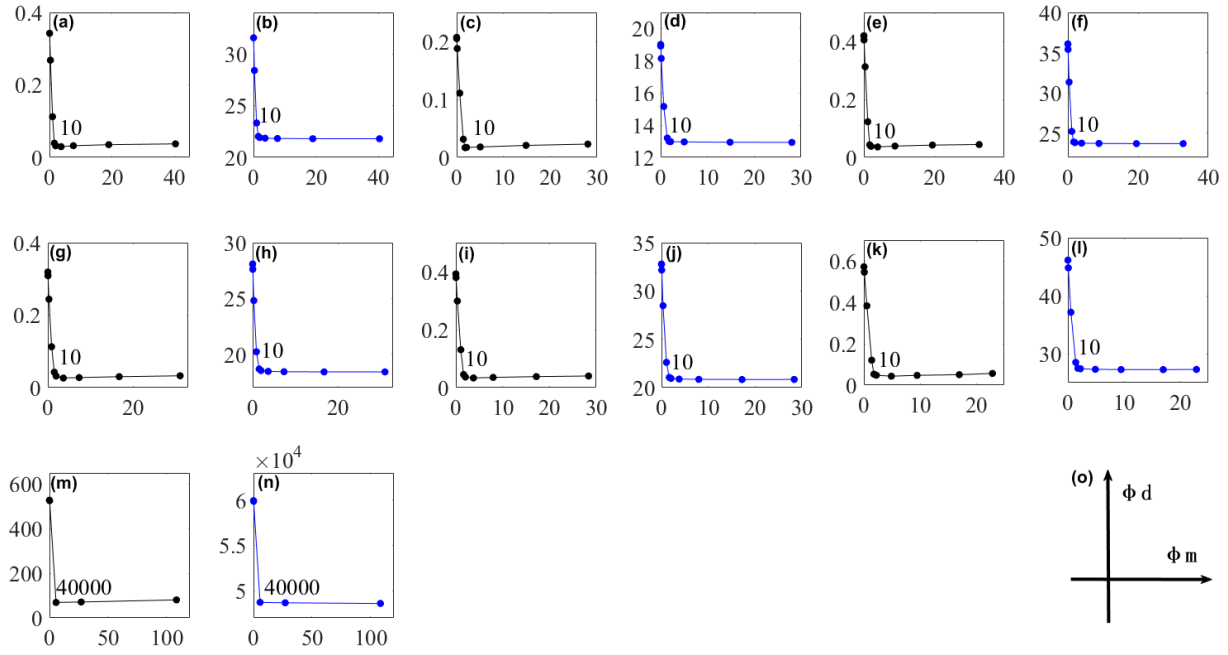


**Figure 10.** Tikhonov curves and the regularization parameter in the wavenumber domain and space domain, separately. The black and blue curves represent the results in the wavenumber domain and spatial domain, respectively. (a),(b)  $g_{xx}$ , (c),(d)  $g_{xy}$ , (e),(f)  $g_{xz}$ , (g),(h)  $g_{yy}$ , (i),(j)  $g_{yz}$ , (k),(l)  $g_{zz}$ , (m),(n)  $g_z$ . The labels of the coordinate axes from Fig. 10a to Fig. 10n are consistent with Fig. 10o.

In the following section, no noise was added to the observed gravity anomalies, making it straightforward to compare the recovered anomalies with the true ones, as illustrated in Fig. 11. It is evident that the residual between the regularized recovered gravity anomaly and the true anomalies is within 2%, as depicted in Fig. 11c. This deviation is acceptable and confirms the validity of the inversion process.

The recovered density model is also compared. By contrasting Fig. 6 with Fig. 11d, it is clear that the horizontal positions are accurately recovered. However, there are notable differences in magnitude, which could potentially

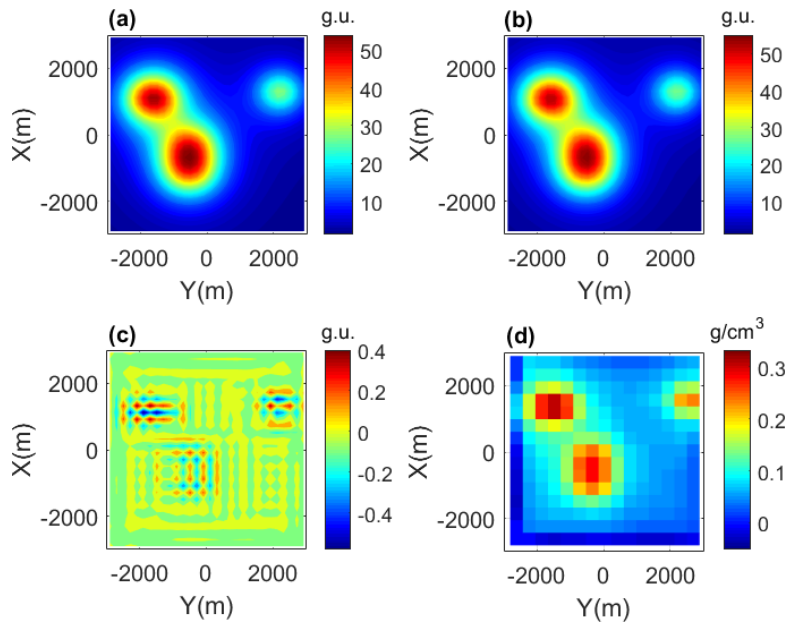


**Figure 11.** Inversion result of model with noise-free. (a) Original gravity anomaly, (b) recovered gravity anomaly, (c) residual of (a) and (b), (d) recovered density model.

be improved with a more sophisticated regularization method. In this paper, our focus is on the accuracy and feasibility of the three-dimensional wavenumber domain inversion method. The use of more complex regularization techniques, such as smooth or bound constraints, is not within our current scope. Essentially, all these regularization techniques can be applied to the wavenumber domain inversion problem. Additionally, the RMS of this inversion is 0.29 g.u..

In addition to the recovered results in Fig. 11, we also compare the inverted spectral characteristics with the theoretical ones. Figs. 12a and 12b depict the power spectrum and phase spectrum of the theoretical gravity anomaly, respectively, while Figs. 12c and 12d show the power spectrum and phase spectrum of the recovered gravity anomaly, respectively. We observe that the power spectral characteristics in Figs. 12a and 12c are identical. Similarly, the phase spectral characteristics in Figs. 12b and 12d are the same.

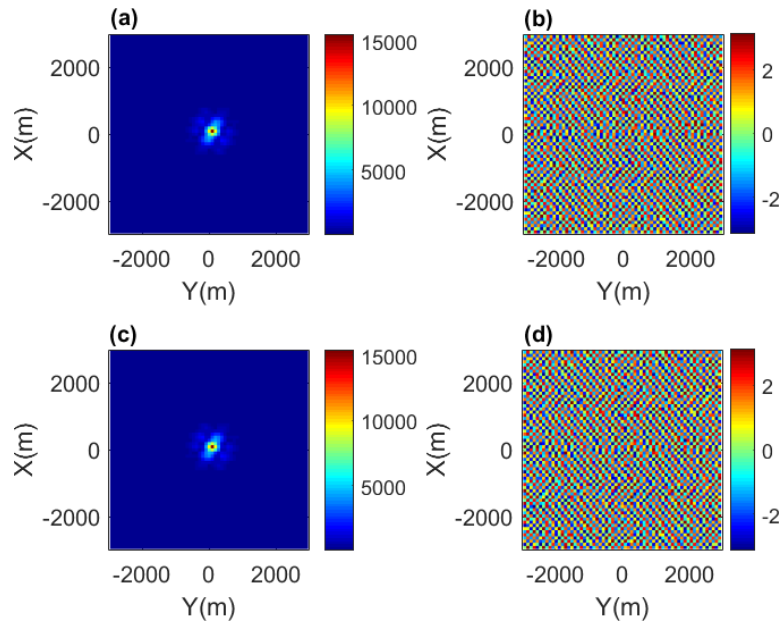


**Figure 12.** Amplitude (a) (c) and phase (b) (d) spectrums of theoretical and recovered model of gravity anomaly.

Then, we further incorporate 5% Gaussian noise in the wavenumber domain, to perform an inversion test. Using the same regularization parameters shown in Fig. 10, the residual characteristics of the inverted gravity anomaly are presented in Fig. 13. Figure 13a shows the anomaly map added with Gaussian noise in the wavenumber domain, while Fig. 13b displays the recovered gravity anomaly. Figure 13c depicts the residual map. When comparing Fig. 11c with Fig. 13c, it is evident that the fitting residual has increased due to noise interference. However, thanks to the regularization parameter, the recovered results are able to mitigate some of the noise interference. Figure 13d shows the recovered density anomaly model, which is visibly impacted by Gaussian noise. Additionally, the RMS is 0.65 g.u..

Figure 14 shows the power spectrum and phase spectrum characteristics with 5% Gaussian interference, where Figs. 14a and 14c are the power spectrum and Figs. 14b and 14d are the phase spectrum.

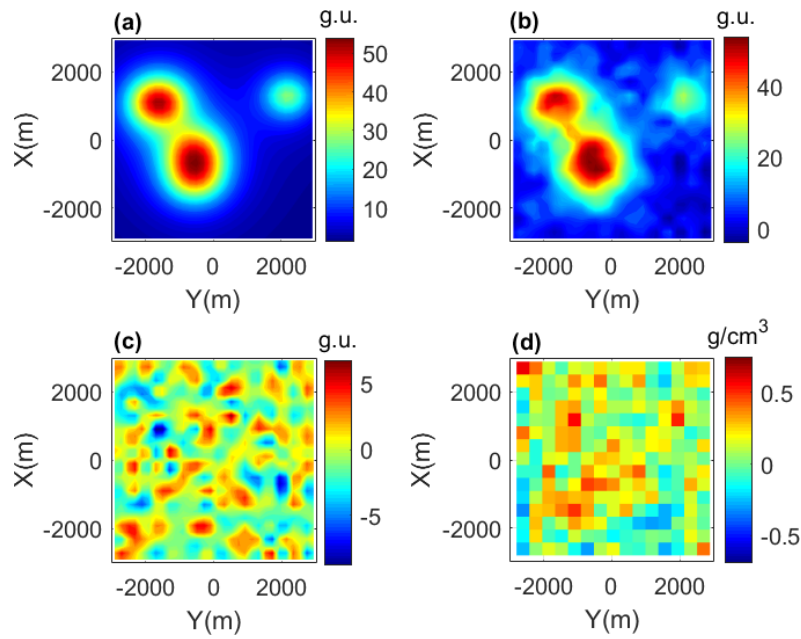


**Figure 13.** Inversion result of model with 5% noise. (a) Original gravity anomaly with 5% noise, (b) recovered gravity anomaly, (c) residual of (a) and (b), (d) recovered density anomaly model.

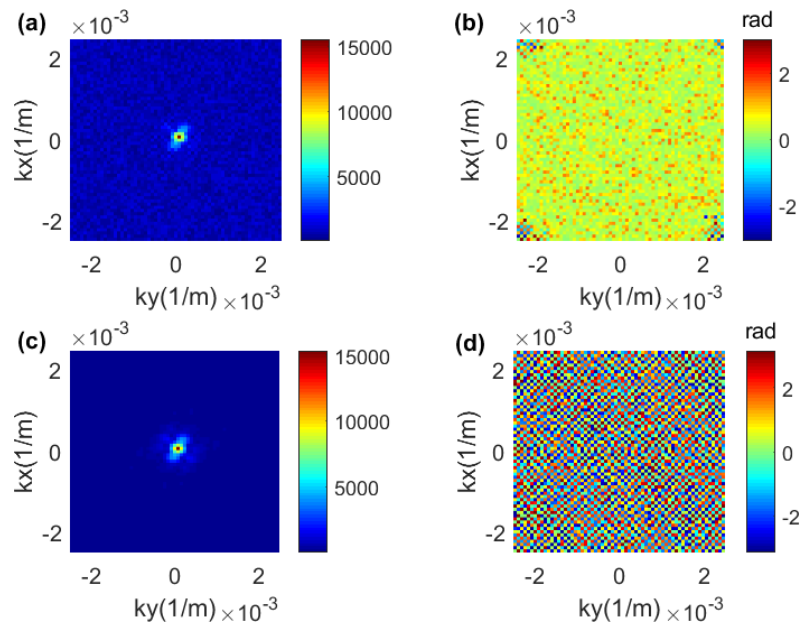
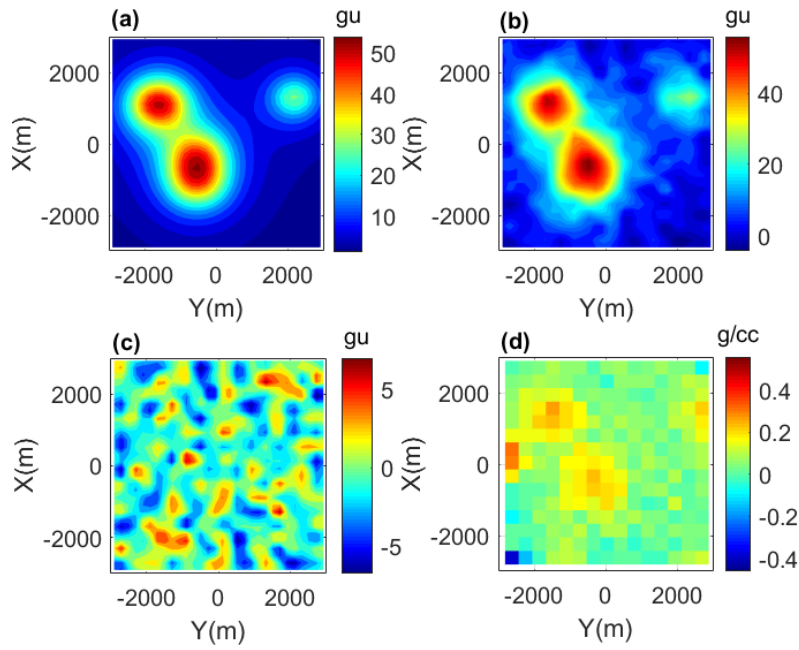


**Figure 14.** Amplitude (a) (c) and phase (b) (d) spectrums of theoretical and inverted model with 5% noise.

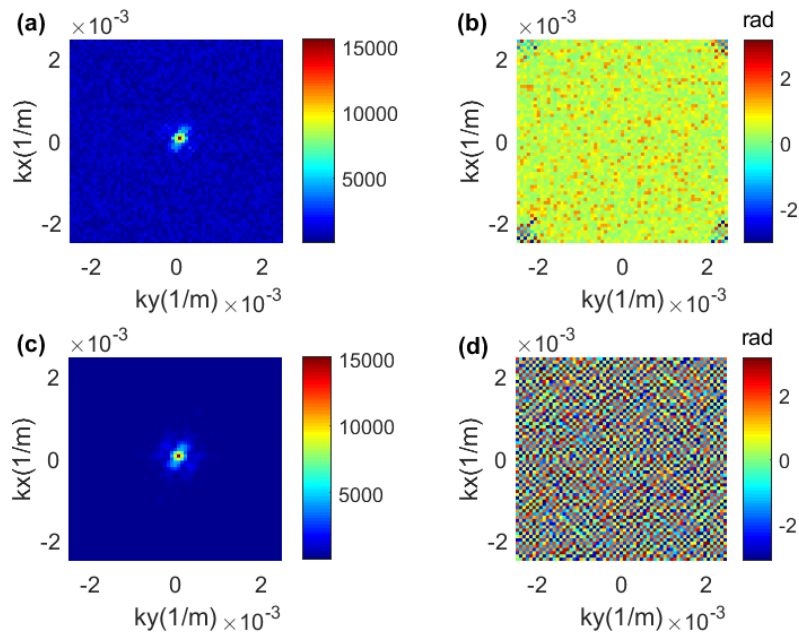
For a deeper comparison of recovered results under noise interference, we selected a regularization parameter of  $4.0e5$  for the inversion process, as depicted in Fig. 15. Figure 15a displays the gravity anomaly map added with Gaussian noise in the wavenumber domain. Figure 15b presents the recovered gravity anomaly, and Fig. 15c shows the residual map. Figure 15d illustrates the recovered density model, which is also influenced by Gaussian noise. When compared to Fig. 13d, Fig. 15d exhibits improved inversion results, accurately representing the three-dimensional spatial distribution of density anomalies. Additionally, the RMS is  $0.6 \text{ g.u.}$ . This underscores the suitability of the regularization method for inverting gravity anomalies within the wavenumber domain.

Figure 16 shows the power spectrum and phase spectrum characteristics with 5% Gaussian interference and new regularized parameter, where Figs. 16a and 16c are the power spectrum and Figs. 16b and 16d are the phase spectrum.

### Gravity-gradient tensor wavenumber inversion

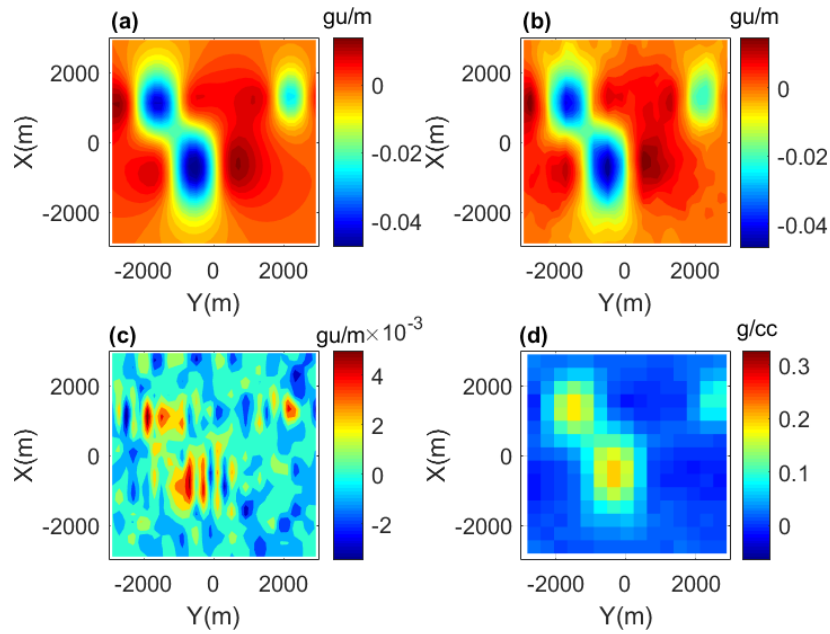


**Figure 15.** The inversion result with 5% noise and  $4.0 \times 10^5$  as the regularization parameter. (a) Original gravity anomaly with 5% noise, (b) recovered gravity anomaly, (c) residual of (a) and (b), (d) recovered density anomaly model.



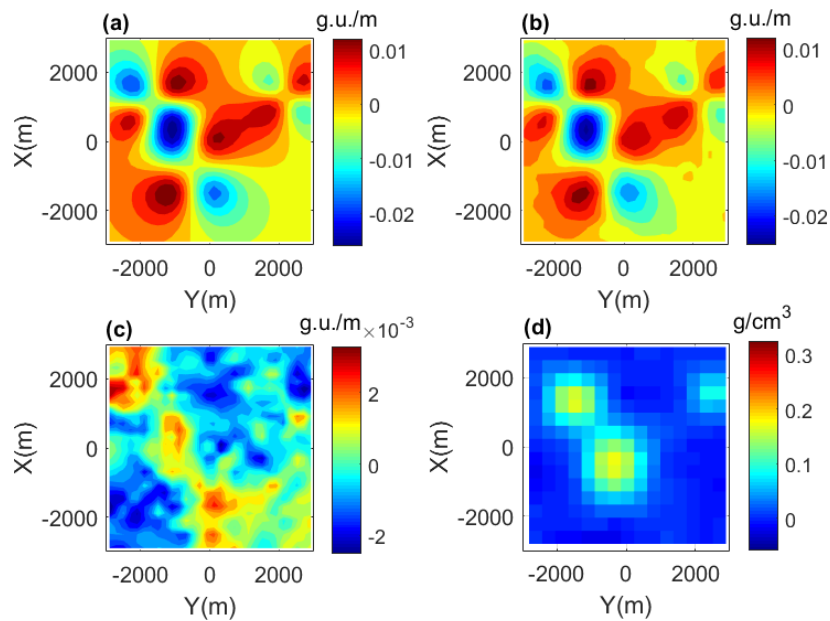
**Figure 16.** Amplitude (a) (c) and phase (b) (d) spectrums of theoretical and recovered model with 5% noise and  $4.0 \times 10^5$  as the regularization parameter.

Then, the full tensor data of the synthetic model 2 are further used to perform inversions of the wavenumber-domain method proposed in this paper, in order to demonstrate the correctness of the proposed inversion method. Figure 17a is the gravity anomaly map with Gaussian noise for  $g_{xx}$  data in the wavenumber domain, Fig. 17b is the recovered  $g_{xx}$  anomaly, and Fig. 17c is the residual map. Figure 17d shows the recovered density anomaly model affected by Gaussian noise. Compared with Fig. 15d, Fig. 17d shows better recovered results and can depict the three-dimensional spatial distribution of density anomalies better. In addition, the RMS is 0.006 g.u./m.



**Figure 17.** The inversion result with 5% noise for gxx data. (a) Original gravity anomaly with 5% noise, (b) recovered gravity anomaly, (c) residual of (a) and (b), (d) recovered density anomaly model.

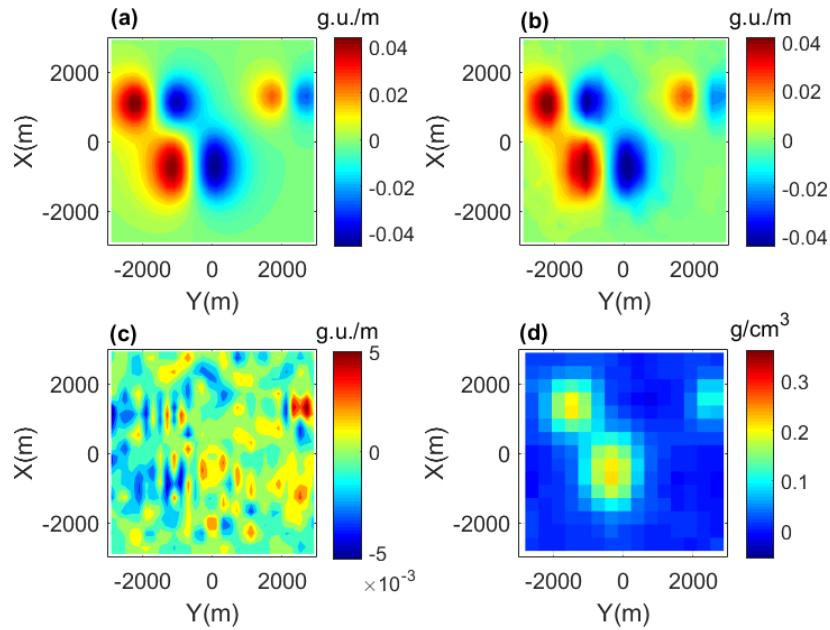
Figure 18a is the gravity anomaly map with Gaussian noise for gxy data in the wavenumber domain, Fig. 18b is the recovered gxx anomaly, and Fig. 18c is the residual map. Figure 18d shows the recovered density anomaly model affected by Gaussian noise. Compared with Fig. 15d, Fig. 18d also shows better recovered results and can depict the three-dimensional spatial distribution of density anomalies better. In addition, the RMS is 0.006 g.u./m.



**Figure 18.** The inversion result with 5% noise for gxy data. (a) Original gravity anomaly with 5% noise, (b) recovered gravity anomaly, (c) residual of (a) and (b), (d) recovered density anomaly model.

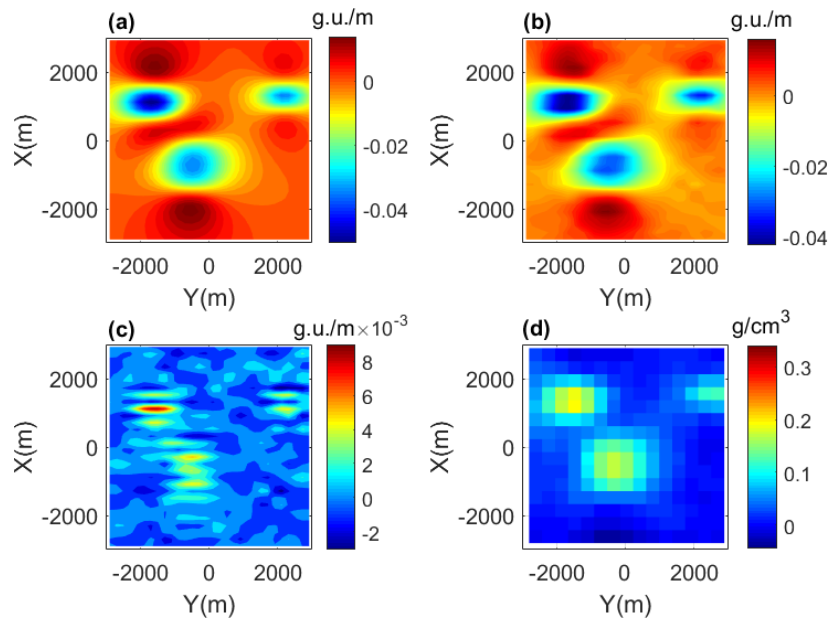
## Gravity-gradient tensor wavenumber inversion

Figure 19 displayed the recovered results of  $gxz$  data, which also demonstrates good outcomes. In addition, the RMS is 0.0045 g.u./m.



**Figure 19.** The inversion result with 5% noise for  $gxz$  data. (a) Original gravity anomaly with 5% noise, (b) recovered gravity anomaly, (c) residual of (a) and (b), (d) recovered density anomaly model.

Additionally, Fig. 20 displayed the inverted results of  $gyy$  data, which also demonstrates good outcomes. In addition, the RMS is 0.0045 g.u./m.



**Figure 20.** The inversion result with 5% noise for  $gyy$  data. (a) Original gravity anomaly with 5% noise, (b) recovered gravity anomaly, (c) residual of (a) and (b), (d) recovered density model.

Furthermore, Fig. 21 displayed the inverted results of gyz data, which also demonstrates good outcomes. In addition, the RMS is 0.0046 g.u./m.

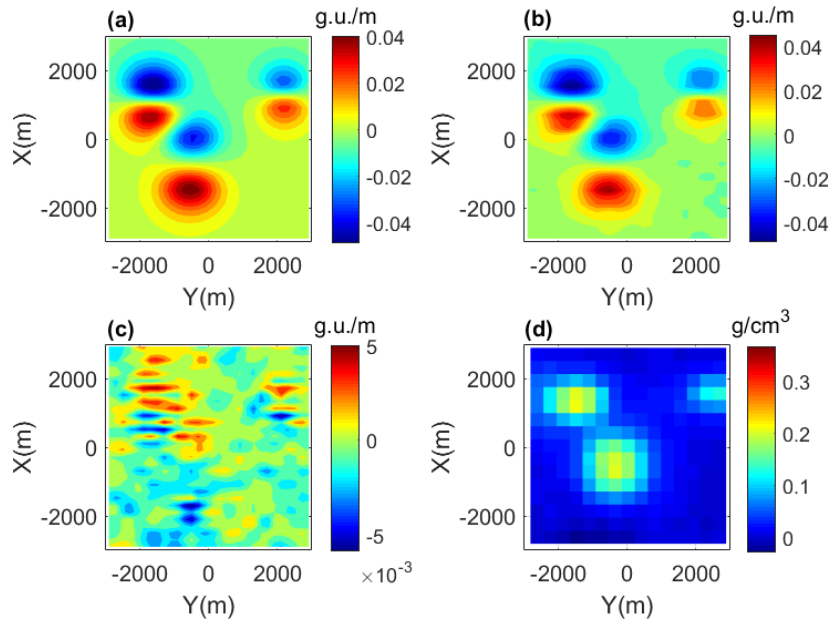


**Figure 21.** The inversion result with 5% noise for gyz data. (a) Original gravity anomaly with 5% noise, (b) recovered gravity anomaly, (c) residual of (a) and (b), (d) recovered density anomaly model.

Utterly, Fig. 22 displayed the recovered results of gzz data, which also acquires good outcomes. In addition, the RMS is 0.0045 g.u./m.

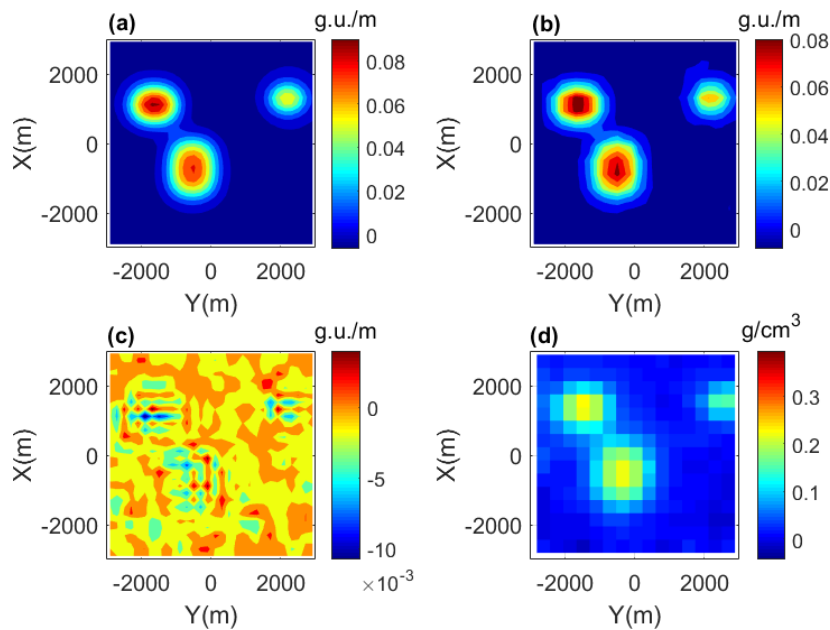


**Figure 22.** The inversion result with 5% noise for gzz data. (a) Original gravity anomaly with 5% noise, (b) recovered gravity anomaly, (c) residual of (a) and (b), (d) recovered density anomaly model.

It's important to note that our prior inversion efforts centered on verifying the accuracy of the wavenumber domain inversion method for gravity anomaly and its gradient tensor data. Next, we'll briefly evaluate the efficiency of the inversion method presented in this paper. We'll refine and test the inversion of the previously used synthetic model 2 data, maintaining the observation network's configuration. The underground source mesh is divided into  $60 \times 60 \times 30$  cells, and the actual density model has also been slightly modified. Following this, we'll conduct inversion testing on gzz data. Figure 23a shows the gzz anomaly map added with Gaussian noise in the frequency domain, Fig. 23b presents the L curve with the optimal regularization parameter of 0.1, Fig. 23c displays the gzz anomaly acquired by recovered density anomaly model, Fig. 23d is the residual map, and Fig. 23e depicts the recovered density anomaly model impacted by Gaussian noise. Compared to Fig. 22d, Fig. 23d also exhibits superior inversion outcomes. In addition, the RMS is 0.008 g.u./m. Crucially, under the current model conditions, the forward computation time in the wavenumber domain is 0.01 seconds, the inversion time in the wavenumber domain is 11.11 seconds, and the forward computation time in the spatial domain is 79.97 seconds. Notably, the computational time for both wavenumber-domain forward and inversion is significantly reduced compared to spatial-domain forward. Clearly, the efficiency of forward and inversion computations in the wavenumber domain has been markedly enhanced.

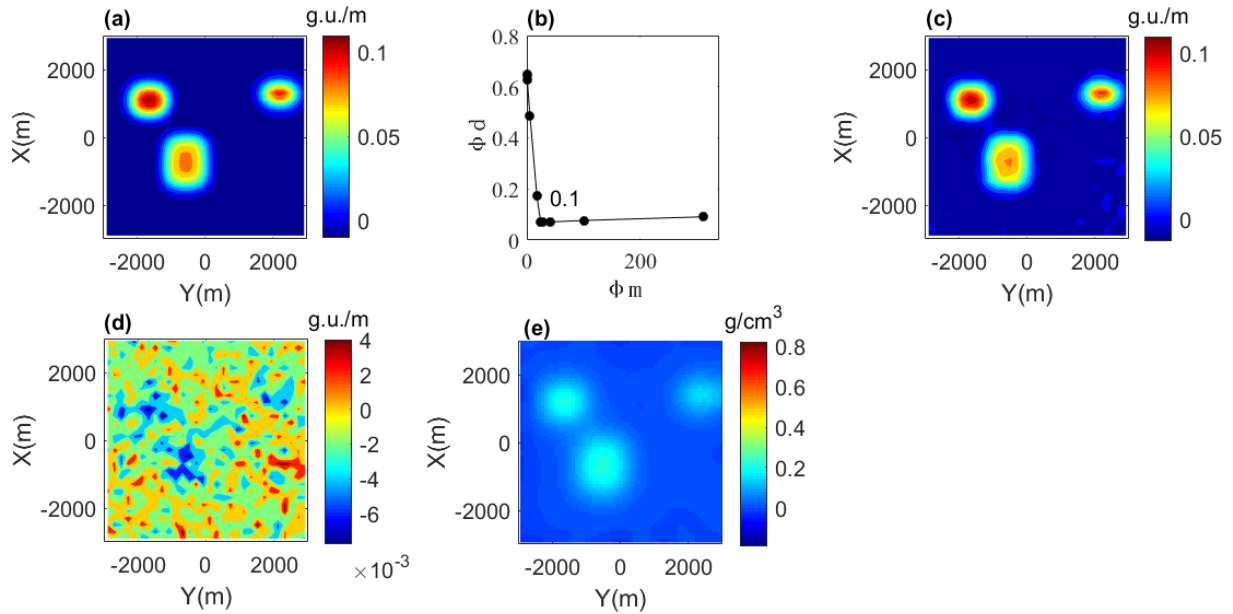


**Figure 23.** The inversion result with 5% noise for gzz data. (a) Original anomaly with 5% noise, (b) L curve, (c) recovered anomaly, (d) residual of (a) and (c), (e) recovered density anomaly model.

We further refined the subdivision of the underground source, achieving a total of  $100 \times 100 \times 50$  meshing units. The observation network configuration remained consistent, while the field source model underwent minor adjustments. Figure 24a displays the forward gzz anomaly in the wavenumber domain, with 5% Gaussian noise applied post-adjustment. Figure 24b presents the L-curve, yielding an optimized regularization parameter of 0.01. Figure 24c illustrates the recovered model's forward gzz anomaly, and Fig. 24d shows the residual. Figure 24e depicts a horizontal slice of the recovered density anomaly model, aligning well with the gzz anomaly distribution in Fig. 24a. In addition, the RMS is 0.0056 g.u./m. Notably, the wavenumber domain forward took 0.03 seconds, the wavenumber domain inversion took 15.05 seconds, and the spatial domain forward took 375.34 seconds. This underscores the efficiency of the inversion method introduced in this paper once more.

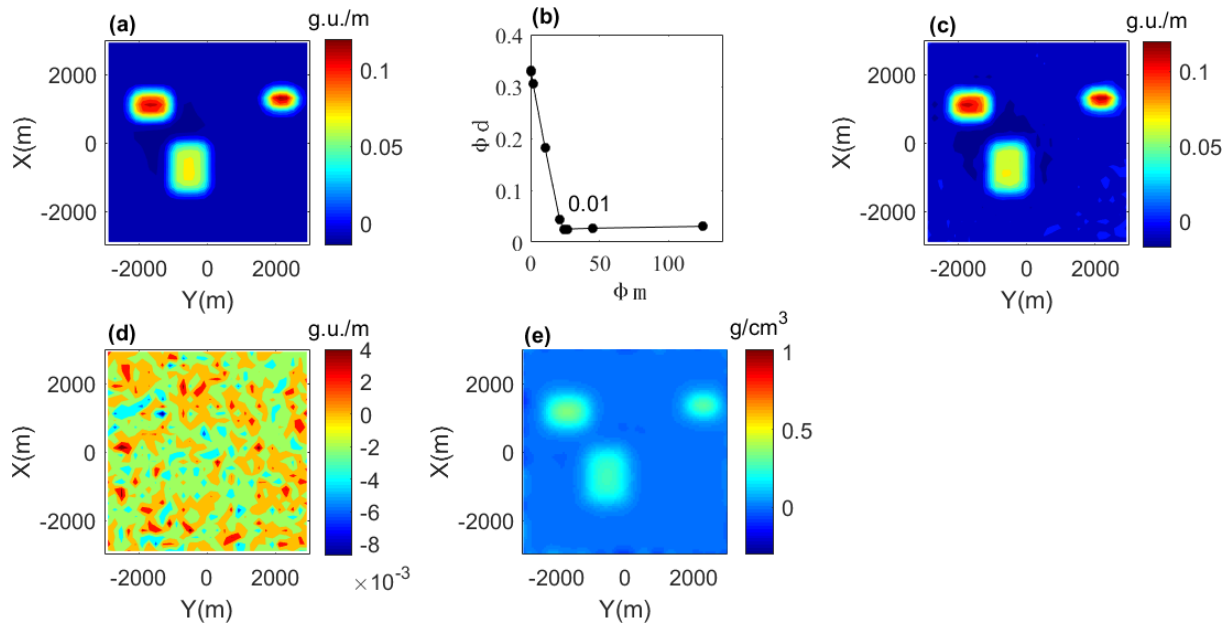


**Figure 24.** The inversion result with 5% noise for gzz data. (a) Original anomaly with 5% noise, (b) L curve, (c) recovered anomaly, (d) residual of (a) and (c), (e) recovered density anomaly model.

To demonstrate the validity of the wavenumber-domain inversion method proposed in this paper, we modified the model in Fig. 24 by altering the property values of two density anomalies to negative values. The inversion was then conducted based on the corresponding forward results. Similarly, we discretized the subsurface sources into  $100 \times 100 \times 50$  grids for inversion. Figure 25a displays the wavenumber-domain forward results of this modified model, Fig. 25b shows the L-curve, Fig. 25c presents the forward results of the inverted wavenumber-domain model, Fig. 25d illustrates the residuals between Figs. 25a and 25c, and Fig. 25e also exhibit horizontal slices of the recovered density anomaly model. In addition, the RMS is 0.0072 g.u./m. The inversion results demonstrate good correspondence with the actual model. Notably, the wavenumber-domain forward required 0.032 seconds, the inversion process took 18.28 seconds, while spatial-domain forward consumed 336.1 seconds. These timing

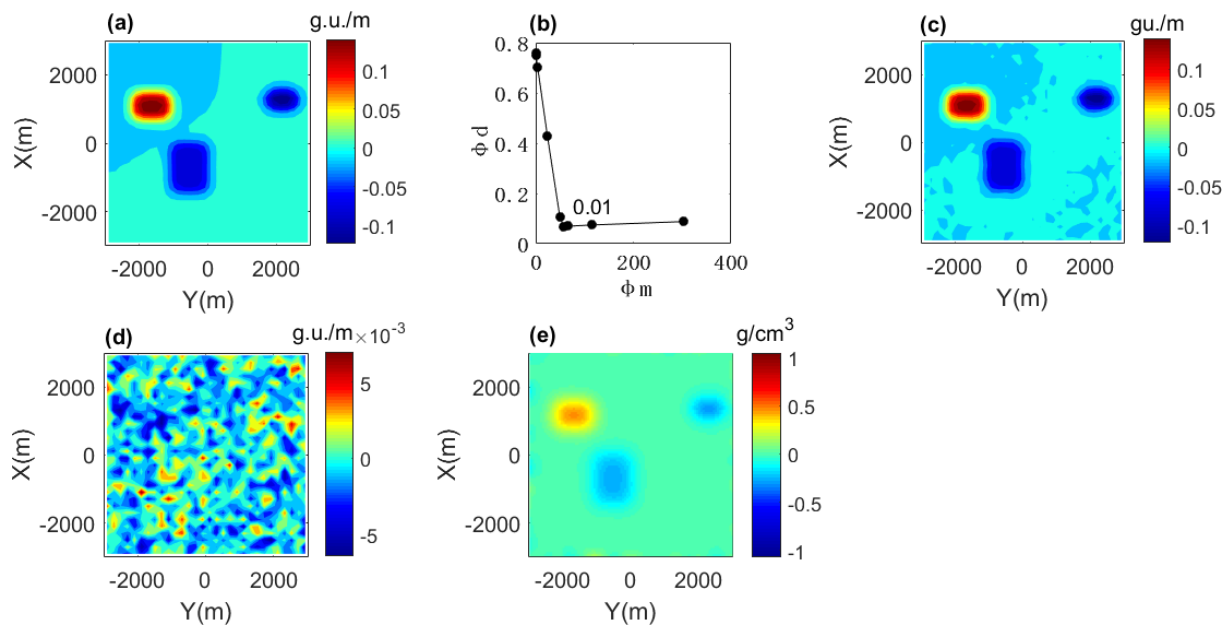


**Figure 25.** The inversion result with 5% noise for gzz data. (a) Original anomaly with 5% noise, (b) L curve, (c) recovered anomaly, (d) residual of (a) and (c), (e) recovered density anomaly model.

comparisons further confirm both the correctness of the wavenumber-domain methodology and its enhanced computational efficiency. Additionally, the successful inversion of models containing both positive and negative anomalies effectively demonstrates the robust general applicability of the proposed method in this paper. In addition, Zhao et al. (2019) divided the subsurface source into  $50 \times 50 \times 25$  grid cells with  $50 \times 50$  observation points, and their inversion time was 5,472.46 seconds. In contrast, in this paper, when the subsurface source was divided into  $100 \times 100 \times 50$  grid cells with  $31 \times 31$  observation points, the inversion time was only 18.28 seconds when running on a standard laptop. Admittedly, the regularization technique employed in the proposed method is relatively simple, which may contribute to some extent to the improved efficiency of the inversion approach. However, the comparison with the inversion time reported by Zhao et al. (2019) effectively demonstrates the superior computational efficiency of the method proposed in this paper.

### 3.2 Application to the field data

Furthermore, the inversion method proposed in this paper will be validated using gravity anomaly data from the Pingbao mining area in Hunan Province, China. The regional gravity field is subtracted from the observed gravity anomaly data. The observation grid consisted of  $24 \times 24$  stations (totaling 576 measurement points), with the measured anomaly data shown in Fig. 26a. Figure 26b shows the optimal regularization parameters of 100 obtained via the L-curve method in the wavenumber domain. Then, the wavenumber-domain inversion was applied to the aforementioned measured gravity anomaly data. We discretized the subsurface space into  $200 \times 200 \times 100$  meshing cells and conducted inversion in the wavenumber domain. The reconstructed density anomaly model are presented in Fig. 26: horizontal slices (Figs. 26c and 26d) and vertical slices of the recovered density anomaly model (Fig. 26e). In addition, the RMS is 0.2 g.u.. The inversion computation time was only 27.2 seconds. The results indicate that the wavenumber-domain inversion effectively reveals the three-dimensional spatial distribution of subsurface density anomalies, demonstrating the feasibility and effectiveness of the proposed wavenumber-domain inversion method in this paper.

It is worth noting that our previous inversion was focused on the correctness of the wavenumber domain inversion method for gravity anomaly and its gradient tensor data. It can be found that the above research results demonstrate that the method proposed in this paper can not only extend the traditional spatial domain regularization inversion

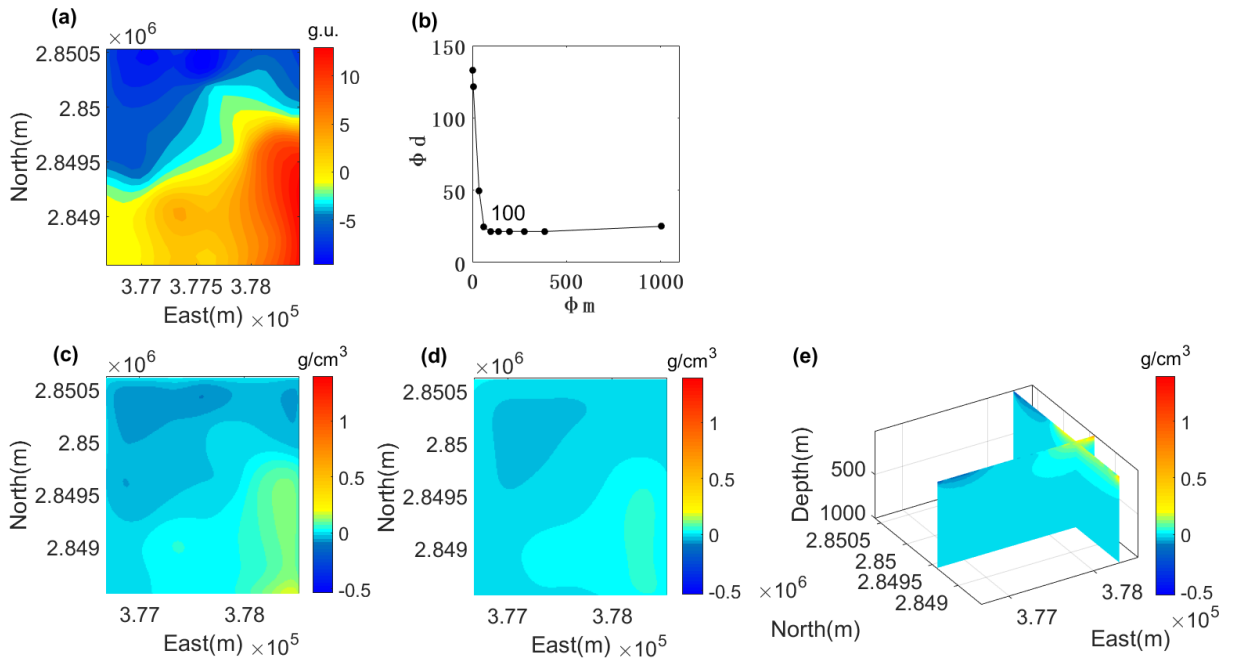


**Figure 26.** Measured gravity anomaly (a), (b) derived via the L-curve method in the wavenumber domain, horizontal slices of the inverted density anomaly model at  $z = 100$  m (c) and  $z = 250$  m (d), and a vertical slices of the recovered density anomaly model (e).

method to the wavenumber domain but also has high efficiency that spatial domain methods cannot match, which is of great value for solving large-scale practical problems in earth science. Since we have employed only relatively simple regularization constraints – solely to demonstrate the validity and effectiveness of the proposed wavenumber-domain forward and inverse techniques for gravity anomaly and its gradient tensor data – depth weighting functions, focusing constraints, and other advanced regularization methods were not applied in this paper. Consequently, the inversion performance still requires further enhancement, which will be the primary focus of our future research.

## 4. Conclusions

This paper introduces a approach for inverting gravity anomaly and its gradient tensor data within the wavenumber domain, utilizing rectangular prismatic models. By factorizing the dense Green's function matrix into a product of three sparse matrices, our method facilitates the use of an optimized algorithm for faster computations. When benchmarked against standard linear inversion techniques, our proposed method demonstrates a substantial improvement in computational efficiency. Tests conducted using synthetic data and field data show that conventional Tikhonov regularization techniques and parameter selection methods are seamlessly adaptable to the wavenumber domain inversion framework. Moreover, in scenarios involving noisy data, regularization parameters can significantly enhance the accuracy of the inverted field source model. Importantly, the wavenumber domain inversion method can incorporate advanced regularization strategies, such as depth weighting, prior constraints, or boundary conditions, for gravity anomaly and its gradient tensor data. Consequently, this method emerges as an efficient and practical tool for potential field inversion. Furthermore, it lays the groundwork for applying more sophisticated regularization constraints and facilitating joint inversion of multiple datasets, which is crucial for addressing real-world challenges, such as inverting gravity data.

**Acknowledgements.** This work was supported by the Key Research Project of Higher Education Institutions in Henan Province, (Grant No. 25A170017), Open Fund of Hebei Key Laboratory of Seismic Dynamics, (Grant No. FZ246104), Henan Province Science and Technology Research Project, (Grant No. 252102320329, 242102321011, 242102320355), National Key R&D Program project of China, (Grant No. 2022YFC3003501), Natural Science Foundation of Beijing (Grant No. 1242033), Open Fund of State Key Laboratory Cultivation Base for Gas Geology and Gas Control (Grant No. WS2024B02), the China Earthquake Administration's Three-in-One Project (Grant No. CEA-SIH-202502009), Natural Science Foundation of Henan, (Grant No. 252300421322, 242300420317), and Henan Province College Students Innovation and Entrepreneurship Training Program, (Grant No. 202511765040, 202511765003, 202511765022). We sincerely thank the two anonymous reviewers for their expert comments that significantly improved our paper. All authors also gratefully acknowledge the editor's valuable assistance in enhancing the manuscript's quality.

## References

- Blakely, R. J. (1995). *Potential Theory in Gravity and Magnetic Applications*, Cambridge Univ. Press, UK, 43-79, 258-308, doi:10.1017/CBO9780511549816.
- Cui, Y. and L. Guo (2019). A wavenumber-domain iterative approach for rapid 3-D imaging of gravity anomalies and gradients, *IEEE Access*, 7, 34179-34188, doi:10.1109/ACCESS.2019.2904717.
- Dai, S. K., Q. R. Chen, K. Li et al. (2020). Three-dimensional numerical modeling of gravity anomaly fields in a mixed spatial-wavenumber domain, *Chin. J. Geophys.*, 63, 5, 2107-2119, doi:10.6038/cjg2020N0294.
- Davis, K. and Y. Li (2011). Fast solution of geophysical inversion using adaptive mesh, space-filling curves and wavelet compression, *Geophys. J. Int.*, 185, 1, 157-166, doi:10.1111/j.1365-246X.2011.04929.x.
- Farquharson, C. G. and D. W. Oldenburg (2004). A comparison of automatic techniques for estimating the regularization parameter in non-linear inverse problems, *Geophys. J. Int.*, 156, 2, 411-425, doi:10.1111/j.1365-246X.2004.02190.x.
- Gray, R. M. (2006). Toeplitz and Circulant Matrices: A Review, *Found. Trends Commun. Inf.*, doi:10.1561/0100000006.

- Hao, Y. and V. Simoncini (2021). The Sherman-Morrison-Woodbury formula for generalized linear matrix equations and applications, *Numer. Linear Algebra Appl.*, 28, 5, e2384, doi:10.1002/nla.2384.
- Hirt, C., S. Claessens, T. Fecher, M. Kuhn et al. (2013). New ultrahigh-resolution picture of Earth's gravity field, *Geophys. Res. Lett.*, 40, 16, 4279-4283, doi:10.1002/grl.50838.
- Hogue, J. D., R. A. Renaut and S. Vatankhah (2020). A tutorial and open-source software for the efficient evaluation of gravity and magnetic kernels, *Comput. Geosci.*, 144, 104575, doi:10.48550/arXiv.1912.06976.
- Hou, Z., X. Wei and D. Huang (2016). Fast density inversion solution for full tensor gravity gradiometry data, *Pure Appl. Geophys.*, 173, 2, 509-523, doi:10.1007/s00024-015-1129-3.
- Hou, Z., B. Sun, P. Qin, C. Zhang et al. (2022). 3D inversion of vertical gravity gradient with multiple graphics processing units based on matrix compression, *Geophysics*, 87, 6, F67-F80, doi:10.1190/geo2021-0472.1.
- Huang, R., Y. Zhang, S. Vatankhah, S. Liu et al. (2022). Inversion of large-scale gravity data with application of Vnet, *Geophys. J. Int.*, 231, 1, 306-318, doi:10.1093/gji/ggac190.
- Jing, L., C. Yao, Y. Yang, M. Xu et al. (2019). Optimization algorithm for rapid 3D gravity inversion, *Appl. Geophys.*, 16, 4, 507-518, doi:10.1007/s11770-019-0781-2.
- Li, K., S. Dai, Q. Chen, Q. Zhang et al. (2019). Three-dimensional numerical modeling of magnetic anomaly fields using an integral method in a mixed spatial-wavenumber domain, *Chin. J. Geophys.*, 62, 11, 4437-4450, doi:10.6038/cjg2019M0633.
- Li, Y. and D. W. Oldenburg (1996). 3-D inversion of magnetic data, *Geophysics*, 61, 2, 394-408, doi:10.1190/1.1443968.
- Li, Y. and D. W. Oldenburg (1998). 3-D inversion of gravity data, *Geophysics*, 63, 1, 109-119, doi:10.1190/1.1444302.
- Li, Y. and D. W. Oldenburg (2003). Fast inversion of large-scale magnetic data using wavelet transforms and a logarithmic barrier method, *Geophys. J. Int.*, 152, 2, 251-265, doi:10.1046/j.1365-246X.2003.01766.x.
- Martin, R., V. Monteiller, D. Komatitsch, S. Perrouty et al. (2013). Gravity inversion using wavelet-based compression on parallel hybrid CPU/GPU systems: application to southwest Ghana, *Geophys. J. Int.*, 195, 3, 1594-1619, doi:10.1093/gji/ggt334.
- Nagy, D. (1966). The gravitational attraction of a right rectangular prism, *Geophysics*, 31, 2, 362-371, doi:10.1190/1.1439779.
- Nagy, D., G. Papp and J. Benedek (2000). The gravitational potential and its derivatives for the prism, *J. Geod.*, 74, 7, 552-560, doi:10.1007/s001900000116.
- Nagy, D., G. Papp and J. Benedek (2002). Corrections to "The gravitational potential and its derivatives for the prism", *J. Geod.*, 76, 8, 475, doi:10.1007/s00190-002-0264-7.
- Oldenburg, D. W. (1974). The inversion and interpretation of gravity anomalies, *Geophysics*, 39, 4, 526-536, doi:10.1190/1.1440444.
- Parker, R. L. (1973). The rapid calculation of potential anomalies, *Geophys. J. R. Astron. Soc.*, 31, 4, 447-455, doi:10.1111/j.1365-246X.1973.tb06513.x.
- Pavlis, N. K., S. A. Holmes, S. C. Kenyon and J. K. Factor (2008). An Earth Gravitational Model to Degree 2160: EGM2008, in *EGU General Assembly 2008*, Vienna, Austria, April 13-18.
- Pavlis, N. K., S. A. Holmes, S. C. Kenyon and J. K. Factor (2012). The development and evaluation of the Earth Gravitational Model 2008 (EGM2008), *J. Geophys. Res. Solid Earth*, 117, B4, B04406, doi:10.1029/2011JB008916.
- Ren, Z., J. Tang, T. Kalscheuer and H. Maurer (2017). Fast 3-D large-scale gravity and magnetic modeling using unstructured grids and an adaptive multilevel fast multipole method, *J. Geophys. Res. Solid Earth*, 122, 1, 79-109, doi:10.1002/2016JB012987.
- Renaut, R. A., J. D. Hogue, S. Vatankhah and S. Liu (2020). A fast methodology for large-scale focusing inversion of gravity and magnetic data using the structured model matrix and the 2-D fast Fourier transform, *Geophys. J. Int.*, 223, 2, 1378-1397, doi:10.1093/gji/ggaa372.
- Sherman, J. and W. J. Morrison (1950). Adjustment of an inverse matrix corresponding to changes in the elements of a given column or a given row of the original matrix, *Ann. Math. Stat.*, 21, 1, 124-127, doi:10.1214/aoms/1177729893.
- Vatankhah, S., R. A. Renaut and V. E. Ardestani (2018). A fast algorithm for regularized focused 3D inversion of gravity data using randomized singular-value decomposition, *Geophysics*, 83, 4, G25-G34, doi:10.1190/geo2017-0386.1.
- Vatankhah, S., S. Liu, R. A. Renaut, X. Hu et al. (2022). An efficient alternating algorithm for the Lp-norm cross-gradient joint inversion of gravity and magnetic data using the 2-D fast Fourier transform, *IEEE Trans. Geosci. Remote Sens.*, 60, 4502016, doi:10.1109/TGRS.2020.3033043.

- Woodbury, M. A. (1950). Inverting Modified Matrices, Memo. Rep. 42, Stat. Res. Group, Princeton Univ., Princeton, NJ, 4.
- Xu, W. and S. Chen (2018). A case study of forward calculations of the gravity anomaly by spectral method for a three-dimensional parameterised fault model, *Comput. Geosci.*, 111, 67-77, doi:10.1016/j.cageo.2017.11.001.
- Yao, C., T. Hao, Z. Guan and Y. Zhang (2003). High-speed computation and efficient storage techniques for 3D inversion of gravity and magnetic data using a genetic algorithm, *Chin. J. Geophys.*, 46, 2, 252-258, doi:10.1002/cjg2.351.
- Yao, C., Y. Zheng and Y. Zhang (2007). 3D inversion of gravity and magnetic anomalies using a stochastic subdomain method, *Chin. J. Geophys.*, 50, 5, 1576-1583, doi:10.3321/j.issn:0001-5733.2007.05.035.
- Zhang, R., T. Li, C. Liu, X. Huang et al. (2022). 3D joint inversion of gravity and magnetic data using data-space and truncated Gauss-Newton methods, *IEEE Geosci. Remote Sens. Lett.*, 19, 4501305, doi:10.1109/LGRS.2021.3077936.
- Zhao, G., B. Chen, L. Uieda, J. Liu et al. (2019). Efficient 3-D large-scale forward modeling and inversion of gravitational fields in spherical coordinates with application to lunar mascons, *J. Geophys. Res. Solid Earth*, 124, 4, 4157-4173, doi:10.1029/2019JB017691.

**\*CORRESPONDING AUTHOR: Sheng LIU,**

Henan University of Urban Construction, Pingdingshan, China

Hebei Key Laboratory of Earthquake Dynamics, Sanhe, China

Institute of Geophysics, China Earthquake Administration, Beijing, China

e-mail: 1500240410@qq.com

© 2025 the Author(s). All rights reserved.

Open Access. This article is licensed under a Creative Commons Attribution 4.0 International